

Robert Babin, BSc

Dimensionality Reduction of 3D Magnetohydrodynamic Equilibria

MASTER'S THESIS

to achieve the university degree of

Diplom-Ingenieur

Master's degree programme: Technical Physics

submitted to

Graz University of Technology

Supervisor

Ass.Prof. Dipl.-Ing. Dr.rer.nat. Christopher Albert

Institute of Theoretical and Computational Physics

in cooperation with the

Max Planck Institute for Plasma Physics

Graz, December 2023

Abstract

Three-dimensional magnetohydrodynamic (MHD) equilibria for stellarators are typically represented with a large number of coefficients. This high dimensionality of the parameter space poses a problem for applications like equilibrium reconstruction, especially if a surrogate model is trained on a collection of sample equilibria. In this thesis, the dimensionality reduction of 3D MHD equilibria using Principal Component Analysis (PCA) is described. The focus lies on the calculation of consistent pressure and current profiles, for which the radial force balance is fulfilled, as well as the quality analysis of the equilibria after the dimensionality reduction. Additionally, low-dimensional 2D equilibria will be discussed in the form of analytical solutions for Solov'ev profiles.

Kurzfassung

Dreidimensionale magnetohydrodynamische (MHD) Gleichgewichte für Stellaratoren werden typischerweise mit einer großen Anzahl an Koeffizienten beschrieben. Diese hohe Dimensionalität des Parameterraums stellt ein Problem für Anwendungen wie die Gleichgewichtsrekonstruktion dar, vor allem wenn ein Surrogatsmodell trainiert wird, basierend auf einer Sammlung von Gleichgewichten. In dieser Abschlussarbeit wird die Dimensionsreduktion von 3D MHD Gleichgewichten mit Hauptkomponentenanalyse (PCA) vorgestellt. Der Fokus liegt dabei auf der Berechnung von konsistenten Druck- und Stromprofilen, für welche das radiale Kräftegleichgewicht erfüllt ist. Ebenso im Fokus liegt die Qualitätsanalyse der Gleichgewichte nach der Dimensionsreduktion. Zusätzlich werden niedrigdimensionale 2D Gleichgewichte, basierend auf analytischen Lösungen für Solov'ev-Profile diskutiert.

Acknowledgements

First and foremost I would like to thank Prof. Christopher Albert for inspiring me to pursue plasma physics and advising me every step along the way. I would also like to thank Prof. Eric Sonnendrücker and Florian Hindenlang at the NMPP Division at the Max Planck Institute for Plasma Physics in Garching for the opportunity to be a guest at the institute for six months. Special thanks to Robert Köberl for being a phenomenal colleague to work with in Garching. Finally, I would like to thank my family for supporting and encouraging me during all my studies.

Contents

| | |
|-----------------------------------------------------------------|-----------|
| Introduction | 1 |
| 1 Theoretical background | 3 |
| 1.1 Plasma models | 3 |
| 1.2 Magnetohydrodynamics | 4 |
| 1.3 Curvilinear coordinate systems | 5 |
| 1.3.1 Cylindrical coordinates | 8 |
| 1.4 Flux coordinates | 9 |
| 1.4.1 Renormalized flux coordinates | 9 |
| 1.5 Variational Moments Equilibrium Code | 10 |
| 1.5.1 Converting to the right-handed coordinates | 11 |
| 1.6 Principal Component Analysis | 12 |
| 1.7 Bayesian Inference | 14 |
| 1.7.1 Gaussian Processes | 14 |
| 1.7.2 Markov Chain Monte Carlo sampling | 15 |
| 2 Grad-Shafranov equation and Solov'ev profiles | 19 |
| 2.1 Derivation of the Grad-Shafranov equation | 19 |
| 2.1.1 Magnetic field | 19 |
| 2.1.2 Current density | 20 |
| 2.1.3 Pressure p | 21 |
| 2.2 Analytical solutions for Solov'ev profiles | 23 |
| 2.2.1 Particular and homogeneous solutions | 24 |
| 2.2.2 Boundary constraints | 24 |
| 3 Radial force balance and consistent profiles | 27 |
| 3.1 Derivation of the radial force balance | 27 |
| 3.2 Toroidal and poloidal current profiles | 29 |
| 3.3 Numerical implementation | 31 |
| 4 Describing MHD equilibrium distributions | 33 |
| 4.1 Equilibrium defining parameters | 33 |
| 4.2 Dimensionality reduction | 34 |
| 4.3 Probability density estimation | 34 |
| 4.4 Quality assessment | 35 |
| 4.4.1 Explained variance ratio | 36 |
| 4.4.2 Reconstruction error of the base quantities | 38 |
| 4.4.3 Reconstruction error of the consistent profiles | 40 |

| | | |
|----------|-------------------------------------------------------|-----------|
| 4.4.4 | Resolution of flux surface integrals | 41 |
| 4.4.5 | Visual interpretation | 41 |
| 4.5 | Improvements using the pressure gradient | 43 |
| 4.6 | Python implementation | 46 |
| 5 | Magnetohydrodynamic equilibrium reconstruction | 49 |
| 5.1 | Reconstruction framework | 49 |
| 5.2 | Equilibrium prior distribution | 51 |
| 5.2.1 | Visual Interpretation | 52 |
| 5.3 | Surrogate models for synthetic diagnostics | 55 |
| 5.4 | Inference | 56 |
| 5.5 | Outlook | 59 |
| | Summary | 61 |
| | List of Figures | 63 |
| | List of Tables | 63 |
| | List of Code Listings | 63 |

Introduction

The ongoing expansion of the global economy necessitates a corresponding rise in electricity consumption, while climate change makes it necessary to transition to carbon-neutral energy sources. Nuclear fusion is a promising future technology, well suited to complement solar and wind power, which both depend on external factors like the weather or time of day. Nuclear fusion can generate large amounts of energy with a small amount of hydrogen and lithium, both of which are abundant on earth. It does not emit greenhouse gases, is comparatively safer than nuclear fission and does not produce as much nuclear waste. However, to build the first fusion power plant, much research still has to be done, to fully understand and be able to control the plasma inside the reactor.

Nuclear fusion happens naturally inside the sun, where hydrogen nuclei fuse in several steps to create helium and release the energy which heats the sun, such that eventually the energy reaches the Earth in the form of light. A similar process, the fusion of deuterium and tritium, two isotopes of hydrogen with one and two neutrons respectively, should power a fusion reactor. To get them to fuse, the Coulomb repulsion between the two nuclei has to be overcome. In magnetic confinement fusion, this is done by heating the fuel to temperatures above 100 million Kelvin and trapping it with magnetic fields to keep it from touching any walls of the reactor. At these temperatures the fuel becomes a plasma, i.e. the electrons separate from the atomic nuclei and the gas becomes strongly conducting and thereby controllable with magnetic fields. When deuterium and tritium fuse, they form helium with an energy of 3.52 MeV and release a neutron with 14.06 MeV [34]. The helium is supposed to keep the plasma heated, while the neutrons escape the plasma and hit the wall, transferring their energy to a cooling fluid that powers a turbine. Additionally, the neutrons should react with lithium at the walls to create the radioactively decaying tritium fuel, such that the whole process only requires deuterium and lithium. One big challenge on the way to a fusion power plant is improving the confinement of the plasma to the point where the helium can provide enough power to balance the heat flux caused by the huge temperature gradients.

One of the simplest plasma models is magnetohydrodynamics (MHD). MHD equilibria are used as the basis of many calculations and also describe the state of the plasma during an experiment. In contrast to tokamaks, which exhibit toroidal symmetry, stellarators, the most promising type of fusion reactor besides tokamaks, necessitate a three-dimensional description of the MHD equilibrium. This 3D nature of stellarators significantly increases computational complexity, requiring the development of data-driven methods to enhance computational efficiency. This thesis discusses the dimensionality reduction of 3D MHD equilibria based on Principal Component Analysis (PCA).

Chapter 1 introduces the ideal MHD model and how solutions to the MHD equations are calculated and described, as well as the basics of dimensionality reduction and Bayesian

Inference. Chapter 2 explores how the toroidal axisymmetry of tokamaks simplifies the MHD equations, leading to the Grad-Shafranov equation. Analytical solutions to this equation will be discussed as well. With the 3D description of MHD equilibria, the radial force balance will be derived in Chapter 3. This allows the calculation of consistent pressure and current profiles in Chapter 4, where the dimensionality reduction of 3D MHD equilibria will be discussed. This is the central part of this thesis and a lot of room is given to the discussion of the quality of the dimensionality reduction. Finally, Chapter 5 presents a framework for 3D equilibrium reconstruction developed by Köberl, Babin, and Albert [18], which relies on the dimensionality reduction described in this thesis.

1 Theoretical background

1.1 Plasma models

Plasma is usually defined as gas which has been heated to such high temperatures that the atoms are ionized [34]. While plasma is macroscopically neutral, the microscopic interactions of matter change significantly. The charged particles will interact by long-range Coulomb interaction and react to electromagnetic fields. This is a fundamental difference to the local nature of thermal collisions and gives rise to many interesting effects, most notably collective phenomena. While plasma is sometimes considered the fourth state of matter, there is no sharp phase transition, but a gradual change as the fraction of ionized particles increases. Plasma comes in several different regimes, across many orders of magnitude, with different chemical compositions, high or low temperatures and densities, large and small length and time scales, as well as quantum or relativistic effects. Plasma used in magnetic confinement fusion is typically rather hot ($\sim 10\text{keV}$), of low density ($\sim 10^{20}\text{m}^{-3}$) and its behaviour is governed by magnetic fields. It is *quasineutral*, which means that any local charge accumulation leading to an electric field is quickly compensated due to the high conductivity of the plasma. The Coulomb potential of each charged particle is screened by the surrounding charges. This decreases the infinite length Coulomb potential to a *Debye-Hückel potential* whose characteristic length is called the *Debye length* λ_D . In *bulk plasma*, the Debye length is much smaller than the size of the plasma volume. In this case, the interactions in the bulk of the plasma dominate over the boundary effects. A plasma is considered weakly coupled if the average number of particles within the Debye sphere, i.e. a sphere of radius λ_D , is much larger than 1. This is fulfilled if the thermal energy of the particles is much larger than the electrostatic Coulomb interaction energy between them. In *weakly coupled plasma*, the collective interactions of many particles govern the behaviour rather than the collisions between two particles. A plasma which is quasineutral, weakly-coupled and a bulk plasma is called an *ideal plasma* [34]. From this point on, only ideal plasmas will be considered.

Due to the collective effects and long-range nature of the electromagnetic fields, modelling the physics of plasmas is challenging. However, with a series of approximations simple plasma models can be derived. The most fundamental starting point for the derivation of plasma models is the *Liouville equation* [25]. For any Hamiltonian system, the probability density in phase space is preserved. With this, the equation of state for an N -particle system can be written as

$$\frac{\partial f_{\alpha}^N}{\partial t} + \sum_{i=1}^N \dot{\mathbf{x}}_i \cdot \frac{\partial f_{\alpha}^N}{\partial \mathbf{x}_i} + \sum_{i=1}^N \dot{\mathbf{v}}_i \cdot \frac{\partial f_{\alpha}^N}{\partial \mathbf{v}_i} = 0, \quad (1.1.1)$$

where $f_\alpha^N(\mathbf{x}_1, \mathbf{v}_1, \dots, \mathbf{x}_N, \mathbf{v}_N, t)$ is the N -particle distribution function for the particle species α , \mathbf{x}_i and \mathbf{v}_i are the position and velocity of the i -th particle and $\dot{\mathbf{x}}_i$ and $\dot{\mathbf{v}}_i$ are the Hamiltonian vector fields for \mathbf{x}_i and \mathbf{v}_i . With $6N + 1$ dimensions this distribution is very impractical. Through marginalizing over all but one particle, under the assumption of identical particles, in a process called the *BBGKY-Hierarchy* [25], the equation of state for the single-particle distribution function $f_\alpha(\mathbf{x}, \mathbf{v}, t)$ can be derived:

$$\frac{\partial f_\alpha}{\partial t} + \dot{\mathbf{x}}_i \cdot \frac{\partial f_\alpha}{\partial \mathbf{x}} + \dot{\mathbf{v}}_i \cdot \frac{\partial f_\alpha}{\partial \mathbf{v}} = \left(\frac{\partial f_\alpha}{\partial t} \right)_{\text{collisions}} \quad (1.1.2)$$

$$\frac{\partial f_\alpha}{\partial t} + \mathbf{v} \cdot \frac{\partial f_\alpha}{\partial \mathbf{x}} + \frac{Z_\alpha e}{m_\alpha} (\mathbf{E} + \mathbf{v} \times \mathbf{B}) \cdot \frac{\partial f_\alpha}{\partial \mathbf{v}} = \left(\frac{\partial f_\alpha}{\partial t} \right)_{\text{collisions}} = \sum_\beta C_{\alpha\beta}. \quad (1.1.3)$$

Here $C_{\alpha\beta}$ is the marginalized collision operator between particle species α and β . This equation is called the *plasma kinetic equation* and when collisions are neglected it is also known as the *Vlasov equation*.

Equation 1.1.3 is the typical starting point for the derivation of different plasma models. The kinetic equation is still $6 + 1$ dimensional and contains two different time and length scales, for motion parallel and perpendicular to the magnetic field. Separating these two scales leads to *gyrokinetic models*. The simplest plasma models can be obtained by calculating the moments of the distribution function f_α with respect to \mathbf{v} . This leads to the *multi-fluid model*, where each species is modelled with a fluid interacting via electromagnetic fields. The theory of such fluid models for plasmas is called *magnetohydrodynamics*.

1.2 Magnetohydrodynamics

Fusion plasmas consist of electrons and ions of light elements like hydrogen. For the following models, only a single ion species will be considered. Furthermore, the electron mass is much smaller than the ion mass, therefore the fluid momentum will be dominated by the motion of the ions. With the same reasoning, the electrons can move much faster than the ions at the same temperature, leading to the assumption of infinite electron conductivity. Together, these properties allow the multi-fluid model to be reduced to the single-fluid, ideal magnetohydrodynamics model, called *ideal MHD*. The equations of this model are [13]:

$$\text{Mass conservation} \quad \frac{\partial \rho}{\partial t} + \nabla \cdot (\rho \mathbf{v}) = 0, \quad (1.2.1)$$

$$\text{Momentum conservation} \quad \rho \frac{d\mathbf{v}}{dt} = \mathbf{J} \times \mathbf{B} - \nabla p, \quad (1.2.2)$$

$$\text{Energy conservation} \quad \frac{d}{dt} \left(\frac{p}{\rho^\gamma} \right) = 0, \quad (1.2.3)$$

$$\text{Ohm's law} \quad \mathbf{E} + \mathbf{v} \times \mathbf{B} = 0, \quad (1.2.4)$$

$$\text{Faraday's law} \quad \nabla \times \mathbf{E} = -\frac{\partial \mathbf{B}}{\partial t}, \quad (1.2.5)$$

$$\text{Ampère's law} \quad \nabla \times \mathbf{B} = \mu_0 \mathbf{J}, \quad (1.2.6)$$

$$\text{and Gauss's law for magnetism} \quad \nabla \cdot \mathbf{B} = 0, \quad (1.2.7)$$

with the fluid velocity \mathbf{v} , mass density ρ , pressure p , current density \mathbf{J} , magnetic field \mathbf{B} , electric field \mathbf{E} , time t and adiabatic index $\gamma = \frac{5}{3}$. The convective derivative is $\frac{d}{dt} = \frac{\partial}{\partial t} + \mathbf{v} \cdot \nabla$.

In many cases, the *MHD equilibrium* is the quantity of interest. An equilibrium is a static solution to the MHD equations, i.e. $\mathbf{v} = 0$ and $\frac{d}{dt} \rightarrow 0$. They fulfil the *MHD equilibrium equations* [13]:

$$\text{Momentum Equation} \quad \nabla p = \mathbf{J} \times \mathbf{B}, \quad (1.2.8)$$

$$\text{Ampère's law} \quad \nabla \times \mathbf{B} = \mu_0 \mathbf{J}, \quad (1.2.9)$$

$$\text{and Gauss's law for magnetism} \quad \nabla \cdot \mathbf{B} = 0. \quad (1.2.10)$$

1.3 Curvilinear coordinate systems

Many physical problems can be simplified by describing them using curvilinear coordinate systems. The quantities of interest can then often be described more simply by leveraging the symmetries of different coordinate systems. Two common examples are cylindrical and spherical coordinates [6].

The three parameters u^1 , u^2 and u^3 are considered *curvilinear coordinates* if any position vector $\mathbf{x} \in \Omega \subset \mathbb{R}^3$ in the 3-dimensional domain Ω , can be expressed in terms of these parameters $\mathbf{x}(u^1, u^2, u^3)$ and the transformation between (u^1, u^2, u^3) and the cartesian coordinates (x, y, z) is invertible and unique. If and only if the transformations

$$x = x(u^1, u^2, u^3), \quad y = y(u^1, u^2, u^3) \quad \text{and} \quad z = z(u^1, u^2, u^3), \quad (1.3.1)$$

have continuous partial derivatives with respect to u^1 , u^2 and u^3 and the determinant of all nine partial derivatives, called the *Jacobian* \mathcal{J} , is non-zero, this transformation is unique and invertible [6]:

$$u^1 = u^1(x, y, z), \quad u^2 = u^2(x, y, z) \quad \text{and} \quad u^3 = u^3(x, y, z). \quad (1.3.2)$$

Two important families of objects for general curvilinear coordinates are *coordinate surfaces*, where one of the three coordinates is held constant, and *coordinate curves*, where two of them are constant. The tangent vectors of the coordinate curves at an arbitrary point \mathbf{x} define the basis at this point. The partial derivatives $\frac{\partial \mathbf{x}}{\partial u^i}$ are tangent to the coordinate curves and are the natural choice for the *tangent-basis vectors* \mathbf{e}_i :

$$\mathbf{e}_1 = \frac{\partial \mathbf{x}}{\partial u^1}, \quad \mathbf{e}_2 = \frac{\partial \mathbf{x}}{\partial u^2} \quad \text{and} \quad \mathbf{e}_3 = \frac{\partial \mathbf{x}}{\partial u^3}. \quad (1.3.3)$$

If the tangent-basis vectors are orthogonal to each other, the coordinate system is called *orthogonal*. In this case, the coordinate curves intersect at right angles [6]. The coordinate system is called *orthonormal* if the *scale factors* or *Lamé coefficients*

$$h_i = |\mathbf{e}_i| \quad (1.3.4)$$

are all equal to 1. Any orthogonal coordinate system with tangent-basis vectors \mathbf{e}_i can be transformed into an orthonormal coordinate system with the basis vectors $\hat{\mathbf{e}}_i$ with

$$\hat{\mathbf{e}}_i = \frac{1}{h_i} \mathbf{e}_i. \quad (1.3.5)$$

Similarly, the normal vectors of the coordinate surfaces at the point \mathbf{x} define a different basis at this point. It can be shown that the gradients ∇u^i of the coordinates are normal vectors of the coordinate surfaces and therefore the natural choice for the *reciprocal*- or *dual-basis vectors* \mathbf{e}^i [6]:

$$\mathbf{e}^1 = \nabla u^1, \quad \mathbf{e}^2 = \nabla u^2 \quad \text{and} \quad \mathbf{e}^3 = \nabla u^3. \quad (1.3.6)$$

The two bases are *reciprocal sets of vectors*, i.e. each vector of one set is orthogonal to two vectors of the other set and the scalar product with the third vector of the other set yields unity:

$$\mathbf{e}^i \cdot \mathbf{e}_j = \delta_j^i = \begin{cases} 1 & i = j \\ 0 & i \neq j \end{cases}, \quad (1.3.7)$$

where δ_j^i is the *Kronecker delta*. Furthermore, the triple products of each basis can be shown to be equal to the Jacobian or its inverse:

$$\mathcal{J} = \mathbf{e}_1 \times \mathbf{e}_2 \cdot \mathbf{e}_3 \quad \text{and} \quad \mathcal{J}^{-1} = \mathbf{e}^1 \times \mathbf{e}^2 \cdot \mathbf{e}^3. \quad (1.3.8)$$

Finally, the reciprocal sets have the inter-relationship [6]:

$$\mathbf{e}^1 = \mathcal{J}^{-1} \mathbf{e}_2 \times \mathbf{e}_3, \quad \mathbf{e}^2 = \mathcal{J}^{-1} \mathbf{e}_3 \times \mathbf{e}_1, \quad \mathbf{e}^3 = \mathcal{J}^{-1} \mathbf{e}_1 \times \mathbf{e}_2, \quad (1.3.9)$$

$$\mathbf{e}_1 = \mathcal{J} \mathbf{e}^2 \times \mathbf{e}^3, \quad \mathbf{e}_2 = \mathcal{J} \mathbf{e}^3 \times \mathbf{e}^1 \quad \text{and} \quad \mathbf{e}_3 = \mathcal{J} \mathbf{e}^1 \times \mathbf{e}^2. \quad (1.3.10)$$

Any vector field \mathbf{D} , at the position \mathbf{x} , can now be expressed as a linear combination of the reciprocal-basis vectors:

$$\mathbf{D} = \left(\mathbf{D} \cdot \frac{\partial \mathbf{R}}{\partial u^1} \right) \nabla u^1 + \left(\mathbf{D} \cdot \frac{\partial \mathbf{R}}{\partial u^2} \right) \nabla u^2 + \left(\mathbf{D} \cdot \frac{\partial \mathbf{R}}{\partial u^3} \right) \nabla u^3 \quad (1.3.11)$$

$$\mathbf{D} = (\mathbf{D} \cdot \mathbf{e}_1) \mathbf{e}^1 + (\mathbf{D} \cdot \mathbf{e}_2) \mathbf{e}^2 + (\mathbf{D} \cdot \mathbf{e}_3) \mathbf{e}^3 \quad (1.3.12)$$

$$\mathbf{D} = D_1 \mathbf{e}^1 + D_2 \mathbf{e}^2 + D_3 \mathbf{e}^3, \quad (1.3.13)$$

where $D_i = \mathbf{D} \cdot \mathbf{e}_i$ are called *covariant components*. Similarly, \mathbf{D} can also be written using the tangent-vector basis:

$$\mathbf{D} = (\mathbf{D} \cdot \nabla u^1) \frac{\partial \mathbf{R}}{\partial u^1} + (\mathbf{D} \cdot \nabla u^2) \frac{\partial \mathbf{R}}{\partial u^2} + (\mathbf{D} \cdot \nabla u^3) \frac{\partial \mathbf{R}}{\partial u^3} \quad (1.3.14)$$

$$\mathbf{D} = (\mathbf{D} \cdot \mathbf{e}^1) \mathbf{e}_1 + (\mathbf{D} \cdot \mathbf{e}^2) \mathbf{e}_2 + (\mathbf{D} \cdot \mathbf{e}^3) \mathbf{e}_3 \quad (1.3.15)$$

$$\mathbf{D} = D^1 \mathbf{e}_1 + D^2 \mathbf{e}_2 + D^3 \mathbf{e}_3, \quad (1.3.16)$$

where $D^i = \mathbf{D} \cdot \mathbf{e}^i$ are called the *contravariant components*. To change the representation from co- to contra-variant, the *metric coefficients* g_{ij} and g^{ij} can be used:

$$D_j = \sum_i D^i g_{ij}, \quad D^j = \sum_i D_i g^{ij}, \quad (1.3.17)$$

$$\text{where } g_{ij} = g_{ji} = \mathbf{e}_i \cdot \mathbf{e}_j \quad \text{and} \quad g^{ij} = g^{ji} = \mathbf{e}^i \cdot \mathbf{e}^j. \quad (1.3.18)$$

The matrix consisting of the metric coefficients g_{ij} is the metric tensor \mathcal{G} and the matrix consisting of g^{ij} is its inverse:

$$\mathcal{G} = [g_{ij}] = [g^{ij}]^{-1}. \quad (1.3.19)$$

The determinant of this matrix is the square of the *Jacobian*

$$\mathcal{J}^2 = g = \det \mathcal{G}. \quad (1.3.20)$$

In orthogonal coordinate systems, the Jacobian is also equal to

$$\mathcal{J} = h_1 h_2 h_3. \quad (1.3.21)$$

In curvilinear coordinate systems, the differential operators also become more complicated. The general form of the divergence $\nabla \cdot \mathbf{D}$ with contravariant components is

$$\nabla \cdot \mathbf{D} = \frac{1}{\mathcal{J}} \sum_{\alpha} \frac{\partial}{\partial \alpha} (\mathcal{J} D^{\alpha}) \quad (1.3.22)$$

and the curl $\nabla \times \mathbf{D}$ with covariant components can be derived by

$$\nabla \times \mathbf{D} = \left(\sum_{\alpha} \nabla \alpha \frac{\partial}{\partial \alpha} \right) \times \left(\sum_{\beta} D_{\beta} \nabla \beta \right) \quad (1.3.23)$$

$$\nabla \times \mathbf{D} = \sum_{\alpha\beta} \nabla \alpha \times \frac{\partial}{\partial \alpha} (D_{\beta} \nabla \beta) \quad (1.3.24)$$

$$\nabla \times \mathbf{D} = \sum_{\alpha\beta} \nabla \alpha \times \nabla \beta \frac{\partial D_{\beta}}{\partial \alpha} + \sum_{\alpha\beta} D_{\beta} \nabla \alpha \times \frac{\partial \nabla \beta}{\partial \alpha} \quad (1.3.25)$$

$$\nabla \times \mathbf{D} = \frac{1}{\mathcal{J}} \sum_{\alpha\beta\gamma} \epsilon_{\alpha\beta\gamma} \frac{\partial D_{\beta}}{\partial \alpha} \mathbf{e}_{\gamma}, \quad (1.3.26)$$

where the second term in 1.3.25,

$$\sum_{\alpha\beta} D_{\beta} \nabla \alpha \times \frac{\partial \nabla \beta}{\partial \alpha} = \sum_{\beta} D_{\beta} \nabla \times \nabla \beta = 0 \quad (1.3.27)$$

cancels as the curl of a gradient always vanishes. Alternatively, by rewriting Equation 1.3.25 differently, the curl can also be expressed as:

$$\nabla \times \mathbf{D} = \sum_{\alpha} \nabla D_{\alpha} \times \nabla \alpha. \quad (1.3.28)$$

1.3.1 Cylindrical coordinates

The right-handed *cylindrical coordinate system* (R, φ, Z) is usually defined with

$$R = \sqrt{X^2 + Y^2}, \quad \varphi = \arctan \frac{Y}{X} \quad \text{and} \quad Z = Z \quad (1.3.29)$$

where (X, Y, Z) are the *cartesian coordinates* with the inverse mapping

$$X = R \cos \varphi, \quad Y = R \sin \varphi \quad \text{and} \quad Z = Z. \quad (1.3.30)$$

With Equations 1.3.29 and 1.3.30 defining a curvilinear coordinate system, the *tangent vector basis* $\mathbf{e}_\alpha = \frac{\partial \mathbf{R}}{\partial \alpha}$ is then

$$\mathbf{e}_R = \begin{pmatrix} \cos \varphi \\ \sin \varphi \\ 0 \end{pmatrix}, \quad \mathbf{e}_\varphi = \begin{pmatrix} -R \cos \varphi \\ R \sin \varphi \\ 0 \end{pmatrix} \quad \text{and} \quad \mathbf{e}_Z = \begin{pmatrix} 0 \\ 0 \\ 1 \end{pmatrix}. \quad (1.3.31)$$

\mathbf{e}_R and \mathbf{e}_Z are already normalized and all three basis vectors are orthogonal. From this, the *scale factors* h_α , *reciprocal basis vectors* \mathbf{e}^α and *orthonormal basis vectors* $\hat{\mathbf{e}}_\alpha$ follow as

$$h_R = 1, \quad h_\varphi = R, \quad h_Z = 1, \quad (1.3.32)$$

$$\mathbf{e}_R = \hat{\mathbf{e}}_R = \mathbf{e}^R, \quad \frac{1}{R} \mathbf{e}_\varphi = \hat{\mathbf{e}}_\varphi = R \mathbf{e}^\varphi \quad \text{and} \quad \mathbf{e}_Z = \hat{\mathbf{e}}_Z = \mathbf{e}^Z. \quad (1.3.33)$$

The *Jacobian* \mathcal{J} is then

$$\mathcal{J} = h_R h_\varphi h_Z = R. \quad (1.3.34)$$

For the contravariant components D^α , the covariant components D_α and the physical components \hat{D}_α the relationship is inverted to the basis vectors:

$$D^R = \hat{D}_R = D_R, \quad R D^\varphi = \hat{D}_\varphi = \frac{1}{R} D_\varphi \quad \text{and} \quad D^Z = \hat{D}_Z = D_Z. \quad (1.3.35)$$

The divergence (Equation 1.3.22) for cylindrical coordinates simplifies to

$$\nabla \cdot \mathbf{D} = \frac{1}{R} \frac{\partial (R \hat{D}_R)}{\partial R} + \frac{1}{R} \frac{\partial \hat{D}_\varphi}{\partial \varphi} + \frac{\partial \hat{D}_Z}{\partial Z}, \quad (1.3.36)$$

while the curl (Equation 1.3.26) written explicitly, gives

$$\nabla \times \mathbf{D} = \left(\frac{1}{R} \frac{\partial \hat{D}_Z}{\partial \varphi} - \frac{\partial \hat{D}_\varphi}{\partial Z} \right) \hat{\mathbf{e}}_R + \left(\frac{\partial \hat{D}_R}{\partial Z} - \frac{\partial \hat{D}_Z}{\partial R} \right) \hat{\mathbf{e}}_\varphi + \frac{1}{R} \left(\frac{\partial (R \hat{D}_\varphi)}{\partial R} - \frac{\partial \hat{D}_R}{\partial \varphi} \right) \hat{\mathbf{e}}_Z. \quad (1.3.37)$$

1.4 Flux coordinates

One convenient choice of coordinates for describing MHD equilibria is *straight field line magnetic flux coordinates* [6]. The right-handed $(\rho, \vartheta^*, \zeta)$ coordinates resemble toroidal coordinates, with ρ being a radius-like coordinate proportional to $\sqrt{\psi}$, where ψ is the toroidal magnetic flux. ρ therefore labels the flux surfaces and is normalized such that it is 0 at the magnetic axis and 1 at the plasma boundary. On these *flux surfaces*, the poloidal magnetic flux χ is also constant. ζ is the toroidal angle, usually equal to φ in cylindrical coordinates. Finally ϑ^* is a poloidal angle-like coordinate, periodic with 2π , but chosen such that the magnetic field \mathbf{B} is straight in these coordinates. The magnetic field is defined by

$$\mathbf{B} = \nabla\psi \times \nabla\vartheta^* - \nabla\chi \times \nabla\zeta. \quad (1.4.1)$$

Contrary to ζ , which is bound to the cylinder coordinates, the offset of ϑ^* can be chosen arbitrarily as only the gradient carries meaning. With Equation 1.3.28, this corresponds to a magnetic vector potential of

$$\mathbf{A} = \psi(\rho) \mathbf{e}^{\vartheta^*} - \chi(\rho) \mathbf{e}^\zeta. \quad (1.4.2)$$

As both the toroidal and the poloidal magnetic flux are constant on a flux surface by definition, their gradient can be rewritten as

$$\nabla\psi = \frac{d\psi}{d\rho} \nabla\rho \quad \text{and} \quad \nabla\chi = \frac{d\chi}{d\rho} \nabla\rho. \quad (1.4.3)$$

Inserted into Equation 1.4.1, the magnetic field can be rewritten as

$$\mathbf{B} = \frac{d\psi}{d\rho} \nabla\rho \times \nabla\vartheta^* - \frac{d\chi}{d\rho} \nabla\rho \times \nabla\zeta \quad (1.4.4)$$

$$\mathcal{J}^* \mathbf{B} = \frac{d\psi}{d\rho} \mathbf{e}_\zeta^* + \frac{d\chi}{d\rho} \mathbf{e}_{\vartheta^*}, \quad (1.4.5)$$

where \mathcal{J}^* is the Jacobian and \mathbf{e}_ζ and \mathbf{e}_{ϑ^*} the tangent-basis vectors for the $(\rho, \vartheta^*, \zeta)$ coordinates. This also shows that \mathbf{B} lies tangent to the flux surfaces. While the contravariant components of \mathbf{B} depend on the Jacobian, $\mathcal{J}^* B^\zeta$ and $\mathcal{J}^* B^{\vartheta^*}$ are the components of the 2-form of \mathbf{B} and are indeed constant. Drawn in the ζ - ϑ^* plane the magnetic field lines are then straight.

1.4.1 Renormalized flux coordinates

Several 3D MHD equilibrium codes like VMEC [15] or DESC [7] modify the straight field line magnetic flux coordinates, primarily to achieve better numerical convergence. The modified coordinate system with the right-handed (ρ, ϑ, ζ) coordinates is very similar to the $(\rho, \vartheta^*, \zeta)$ coordinates presented above, only the ϑ coordinate is different. The poloidal angle ϑ is defined as

$$\vartheta = \vartheta^* - \lambda(\rho, \vartheta, \zeta), \quad (1.4.6)$$

where λ is called the renormalization parameter. The magnetic field from Equation 1.4.4 becomes

$$\mathbf{B} = \frac{d\psi}{d\rho} \nabla \rho \times \nabla (\vartheta + \lambda) - \frac{d\chi}{d\rho} \nabla \rho \times \nabla \zeta. \quad (1.4.7)$$

Codes like VMEC also typically solve for the MHD equilibrium in the form of the inverse coordinate transform. That is, they solve for $R(\rho, \vartheta, \zeta)$, $Z(\rho, \vartheta, \zeta)$ and $\lambda(\rho, \vartheta, \zeta)$, which define the flux surfaces and therefore the magnetic field. Two crucial elements for calculations in curvilinear coordinates are the Jacobian \mathcal{J} and the elements of the metric tensor g_{ij} . The Jacobian for the (ρ, ϑ, ζ) coordinate system is:

$$\mathcal{J} = \mathbf{e}_\rho \cdot \mathbf{e}_\vartheta \times \mathbf{e}_\zeta \quad (1.4.8)$$

$$\mathcal{J} = \frac{\partial \mathbf{x}}{\partial \rho} \cdot \frac{\partial \mathbf{x}}{\partial \vartheta} \times \frac{\partial \mathbf{x}}{\partial \zeta} \quad (1.4.9)$$

$$\mathcal{J} = \left(\frac{\partial R}{\partial \rho} \frac{\partial \mathbf{x}}{\partial R} + \frac{\partial Z}{\partial \rho} \frac{\partial \mathbf{x}}{\partial Z} \right) \cdot \left(\frac{\partial R}{\partial \vartheta} \frac{\partial \mathbf{x}}{\partial R} + \frac{\partial Z}{\partial \vartheta} \frac{\partial \mathbf{x}}{\partial Z} \right) \times \left(\frac{\partial R}{\partial \zeta} \frac{\partial \mathbf{x}}{\partial R} + \frac{\partial \varphi}{\partial \zeta} \frac{\partial \mathbf{x}}{\partial \varphi} + \frac{\partial Z}{\partial \zeta} \frac{\partial \mathbf{x}}{\partial Z} \right) \quad (1.4.10)$$

$$\mathcal{J} = \frac{\partial R}{\partial \rho} \mathbf{e}_R \cdot \frac{\partial Z}{\partial \vartheta} \mathbf{e}_Z \times \frac{\partial \varphi}{\partial \zeta} \mathbf{e}_\varphi + \frac{\partial Z}{\partial \rho} \mathbf{e}_Z \cdot \frac{\partial R}{\partial \vartheta} \mathbf{e}_R \times \frac{\partial \varphi}{\partial \zeta} \mathbf{e}_\varphi \quad (1.4.11)$$

$$\mathcal{J} = \mathcal{J}_{R\varphi Z} \left(\frac{\partial R}{\partial \vartheta} \frac{\partial \varphi}{\partial \zeta} \frac{\partial Z}{\partial \rho} - \frac{\partial R}{\partial \rho} \frac{\partial \varphi}{\partial \zeta} \frac{\partial Z}{\partial \vartheta} \right) \quad (1.4.12)$$

$$\mathcal{J} = R \left(\frac{\partial R}{\partial \vartheta} \frac{\partial Z}{\partial \rho} - \frac{\partial R}{\partial \rho} \frac{\partial Z}{\partial \vartheta} \right), \quad (1.4.13)$$

where $\mathcal{J}_{R\varphi Z} = \mathbf{e}_R \cdot \mathbf{e}_\varphi \times \mathbf{e}_Z = R$ is the Jacobian for cylindrical coordinates (see Section 1.3.1) and the toroidal angles were defined to be equal with $\zeta = \varphi$. The angular coefficients of the metric tensor are

$$g_{\vartheta\vartheta} = \mathbf{e}_\vartheta \cdot \mathbf{e}_\vartheta = \frac{\partial R}{\partial \vartheta} \frac{\partial R}{\partial \vartheta} + \frac{\partial Z}{\partial \vartheta} \frac{\partial Z}{\partial \vartheta} \quad (1.4.14)$$

$$g_{\vartheta\zeta} = g_{\zeta\vartheta} = \mathbf{e}_\vartheta \cdot \mathbf{e}_\zeta = \frac{\partial R}{\partial \vartheta} \frac{\partial R}{\partial \zeta} + \frac{\partial Z}{\partial \vartheta} \frac{\partial Z}{\partial \zeta} \quad (1.4.15)$$

$$g_{\zeta\zeta} = \mathbf{e}_\zeta \cdot \mathbf{e}_\zeta = \frac{\partial R}{\partial \zeta} \frac{\partial R}{\partial \zeta} + R^2 + \frac{\partial Z}{\partial \zeta} \frac{\partial Z}{\partial \zeta}, \quad (1.4.16)$$

while the other three coefficients $g_{\rho\rho}$, $g_{\rho\vartheta}$ and $g_{\rho\zeta}$ are not needed in the following chapters, as the radial components vanish for most quantities of interest, like \mathbf{B} and \mathbf{J} .

1.5 Variational Moments Equilibrium Code

The *Variational Moments Equilibrium Code* (VMEC) by Hirshman and Whitson [15] is a widespread 3D MHD equilibrium solver. The equilibrium calculated by VMEC is described by the inverse coordinate representation $\mathbf{x}(\rho, \theta, \zeta) = (R, \varphi, Z)$. Here (ρ, θ, ζ) are similar to the magnetic flux coordinates described in Section 1.4.1, with the difference that $\theta = -\vartheta$ and (ρ, θ, ζ) are therefore left-handed coordinates. (R, φ, Z) are the usual cylindrical coordinates described in Section 1.3.1. The inverse coordinate representation

in VMEC for $R(\rho, \theta, \zeta)$ and $Z(\rho, \theta, \zeta)$ utilizes a Fourier basis for the poloidal and toroidal angles, along with a finite difference approach for the radial direction. The radial grid is linearly spaced within the toroidal flux $\psi \propto \rho^2$. The poloidal angle θ is related to the straight field line angle $-\vartheta^* = \theta^* = \theta + \lambda$ through the renormalization parameter $\lambda(\rho, \theta, \zeta)$ which is also given as a Fourier series in θ and ζ , but placed radially on the midpoints between the radial grid for R and Z . This secondary grid is called the *half mesh*. λ is used to guarantee fast convergence of VMEC and reduce the number of modes needed for an accurate representation. Additionally the rotational transform profile

$$\iota(\rho) = \frac{d\chi}{d\psi} = \frac{B^{\theta^*}}{B\zeta} \quad (1.5.1)$$

relates the poloidal and toroidal magnetic flux and is described by points on the full mesh. Finally the total toroidal flux ψ_0 is a scalar, which maps the radial coordinate to the toroidal magnetic flux and the *number of field periods* N_{FP} describe a global toroidal symmetry, which constrains the toroidal mode numbers to multiples of N_{FP} . Taking into account the *stellarator symmetry*, the basis for R , Z and λ is:

$$R(\rho, \theta, \zeta) = \sum_{m=0}^M \sum_{n=-N}^N R_{mn}(\rho) \cos(m\theta - nN_{FP}\zeta), \quad (1.5.2)$$

$$Z(\rho, \theta, \zeta) = \sum_{m=0}^M \sum_{n=-N}^N Z_{mn}(\rho) \sin(m\theta - nN_{FP}\zeta) \quad (1.5.3)$$

$$\text{and } \lambda(\rho, \theta, \zeta) = \sum_{m=0}^M \sum_{n=-N}^N \lambda_{mn}(\rho) \sin(m\theta - nN_{FP}\zeta), \quad (1.5.4)$$

where $R_{mn}(\rho)$, $Z_{mn}(\rho)$ and $\lambda_{mn}(\rho)$ are interpolated between the values of R_{kmn} , Z_{kmn} and $\bar{\lambda}_{lmn}$ on the full mesh ρ_k and half mesh $\bar{\rho}_l$ respectively. Therefore a VMEC equilibrium is fully described by ψ_0 , R_{kmn} , Z_{kmn} , $\bar{\lambda}_{lmn}$, ι_k and N_{FP} . All other equilibrium quantities can be calculated from these parameters.

VMEC solves for these parameters by minimizing the total plasma potential energy

$$W = \int_V \frac{B^2}{2\mu_0} + \frac{p}{\gamma - 1} d\mathbf{x}, \quad (1.5.5)$$

using a gradient descent algorithm.

1.5.1 Converting to the right-handed coordinates

For the (ρ, θ, ζ) coordinate system, the poloidal angle increases in the counterclockwise direction when viewed from the front and the toroidal angle ζ increases counterclockwise when viewed from above. In contrast, in the right-handed flux coordinate system (ρ, ϑ, ζ) , the poloidal angle $\vartheta = -\theta$ increases in the clockwise direction when viewed from the front. The basis functions 1.5.2 to 1.5.4 can be converted to the right-handed coordinate system

with:

$$R(\rho, \vartheta, \zeta) = \sum_{m=0}^M \sum_{n=-N}^N R_{mn}^r(\rho) \cos(m\vartheta - nN_{FP}\zeta) \Rightarrow R_{mn}^r = R_{m(-n)}, \quad (1.5.6)$$

$$Z(\rho, \vartheta, \zeta) = \sum_{m=0}^M \sum_{n=-N}^N Z_{mn}^r(\rho) \sin(m\vartheta - nN_{FP}\zeta) \Rightarrow Z_{mn}^r = -Z_{m(-n)}^l, \quad (1.5.7)$$

$$\text{and } \lambda(\rho, \vartheta, \zeta) = \sum_{m=0}^M \sum_{n=-N}^N \lambda_{mn}^r(\rho) \sin(m\vartheta - nN_{FP}\zeta) \Rightarrow \lambda_{mn}^r = \lambda_{m(-n)}^l. \quad (1.5.8)$$

Here λ has also switched the sign, such that $\vartheta = \vartheta^* + \lambda(\rho, \vartheta, \zeta)$ holds. While the toroidal flux ψ stays the same, the poloidal flux χ and the rotational transform profile ι also need to change their respective sign. Additionally, the convention for VMEC coefficients is, that for the case of $m = 0$, only positive values of n are used, such that all $R_{0n} = Z_{0n} = \lambda_{0n} = 0$ with $n < 0$. To keep this convention, the coefficients for $m = 0$ need to be:

$$R_{0n}^r(\rho) = R_{0n}(\rho), \quad Z_{0n}^r(\rho) = Z_{0n}(\rho) \quad \text{and} \quad \lambda_{0n}^r(\rho) = -\lambda_{0n}(\rho). \quad (1.5.9)$$

1.6 Principal Component Analysis

Dimensionality reduction is the process of finding a subspace, called the *latent space*, which requires less dimensions, but still retains most of the information of the target distribution. A very common, but powerful method for dimensionality reduction is *Principal Component Analysis* (PCA).

PCA finds a linear transformation which diagonalizes the covariance matrix of the data. This step does not reduce the dimensionality and is lossless up to machine precision. Next, the basis of eigenvectors, called *principal components*, is truncated to the L highest eigenvalues. This step retains a specified amount of the variance and reduces the dimensionality to the most important dimensions to explain the data variance. Typically, the majority of the variance can be explained with the first few principal components and further dimensions give diminishing returns. PCA is particularly fast, as calculating the eigenvectors of the covariance matrix is equivalent to performing a *Singular Value Decomposition* (SVD) on the centered data matrix, for which several fast algorithms exist.

Let Q be the data matrix of dimensions $(F \times S)$, where F is the total number of features and S the number of samples. The covariance matrix Σ is a $(F \times F)$ matrix defined by

$$\Sigma = \frac{1}{S} (Q - \boldsymbol{\mu})(Q - \boldsymbol{\mu})^T, \quad (1.6.1)$$

where $\boldsymbol{\mu} = \frac{1}{S} \sum_{s=0}^{S-1} \mathbf{q}_s$ is the mean vector of length F .

The first step of PCA is the eigenvalue decomposition of the covariance matrix Σ :

$$\Sigma = P \Lambda P^T, \quad (1.6.2)$$

where P is the $(F \times F)$ matrix of the eigenvectors¹ \mathbf{p} , called *principal components* in this setting and Λ is the diagonal $(F \times F)$ matrix of eigenvalues. The eigenvalues Λ_l are called the *explained variance*, as they describe the contribution of each principal component to the total variance σ^2 of the distribution:

$$\sigma^2 = \sum_{ij=0}^{F-1} \Sigma_{ij} = \sum_{l=0}^{F-1} \Lambda_l. \quad (1.6.3)$$

The PCA approximation is done by truncating the number of principal components, such that most of the variance is preserved. The L largest eigenvectors are kept and they form a vector basis of the latent space. The covariance and data matrices are approximated with

$$\Sigma = P\Lambda P^T \approx \tilde{P}\tilde{\Lambda}\tilde{P}^T \quad (1.6.4)$$

$$\text{and } Q = \boldsymbol{\mu} + Pc \approx \boldsymbol{\mu} + \tilde{P}\tilde{c} = \tilde{Q}, \quad (1.6.5)$$

where $\tilde{\Lambda}$ is the truncated, diagonal $(L \times L)$ matrix of eigenvalues, \tilde{P} the truncated $(F \times L)$ matrix of principal components, c the $(F \times S)$ matrix of coefficients in the eigenbasis of Σ and \tilde{c} the $(L \times S)$ matrix of coefficients in the truncated eigenbasis, which means that \tilde{c} is simply a truncated form of c . The coefficients c are determined with the inverse transformation

$$c = P^T (Q - \boldsymbol{\mu}) \quad \text{and} \quad \tilde{c} = \tilde{P}^T (Q - \boldsymbol{\mu}) = \tilde{P}^T (\tilde{Q} - \boldsymbol{\mu}). \quad (1.6.6)$$

The *explained variance ratio*

$$\sigma_{evr,l}^2 = \frac{\Lambda_l}{\sigma^2} \quad (1.6.7)$$

is a measure of quality for the dimensionality reduction. Similarly the *unexplained variance ratio* for a reduction to L latent dimensions is

$$\sigma_{uvr}^2(L) = 1 - \sum_{l=0}^{L-1} \sigma_{evr,l}^2, \quad (1.6.8)$$

which measures the fraction of the variance that is discarded in the dimensionality reduction.

Finally, in practice PCA is computed with a more efficient Singular Value Decomposition (SVD) of the centered data matrix $Q - \boldsymbol{\mu}$, instead of the Eigenvalue Decomposition of the covariance matrix. In this case both decompositions are equivalent as

$$Q - \boldsymbol{\mu} = P\sqrt{\Lambda}V^T \quad (1.6.9)$$

$$(Q - \boldsymbol{\mu})(Q - \boldsymbol{\mu})^T = P\sqrt{\Lambda}V^TV\sqrt{\Lambda}P^T \quad (1.6.10)$$

$$\Sigma = P\Lambda P^T \quad (1.6.11)$$

and the transformation matrix V of the SVD is unitary.

¹ P is an orthogonal matrix as Σ is real and symmetric. Therefore P is also unitary, i.e. $P^{-1} = P^T$ and the principal components p are real and orthonormal.

1.7 Bayesian Inference

A common problem with experiments in physics is that the quantities of interest \mathbf{Q} cannot be measured directly. In many cases there exist models from first principles, with which the measurable quantities \mathbf{d} can be calculated from the hidden quantities \mathbf{Q} , but there are no models for the inverse direction. Such problems are called *inverse problems* and the method of solving them based on *Bayesian probability theory* is called *Bayesian Inference* [23].

At the center of Bayesian probability theory is *Bayes' theorem*

$$p(\mathbf{Q} | \mathbf{d}, \mathcal{I}) = \frac{p(\mathbf{d} | \mathbf{Q}, \mathcal{I}) p(\mathbf{Q}, \mathcal{I})}{p(\mathbf{d}, \mathcal{I})}. \quad (1.7.1)$$

The probability distribution $p(\mathbf{Q} | \mathcal{I})$ is the *prior distribution* of the hidden quantities, encoding all previous knowledge and assumptions \mathcal{I} about them. The conditional probability distribution $p(\mathbf{d} | \mathbf{Q}, \mathcal{I})$ is called the *likelihood function* and describes the *forward model* from \mathbf{Q} to \mathbf{d} , as well as the measurement uncertainty. In particular for a forward model $f(\mathbf{Q})$ and a symmetric measurement uncertainty $p(\epsilon)$, the likelihood is simply

$$p(\mathbf{d} | \mathbf{Q}, \mathcal{I}) = p(\epsilon = |\mathbf{d} - f(\mathbf{Q})|). \quad (1.7.2)$$

The normalizing factor

$$p(\mathbf{d} | \mathcal{I}) = \int p(\mathbf{d} | \mathbf{Q}, \mathcal{I}) p(\mathbf{Q} | \mathcal{I}) d\mathbf{Q} \quad (1.7.3)$$

is called the *evidence* and lastly, the conditional probability distribution $p(\mathbf{Q} | \mathbf{d}, \mathcal{I})$ is the *posterior distribution*, describing the probability distribution for the hidden quantities \mathbf{Q} , given the measured quantities \mathbf{d} under the assumptions and prior information \mathcal{I} [23]. Under favorable conditions, the posterior distribution can be analytically calculated using *Gaussian Processes*. Another possibility is the approximation using *Markov Chain Monte Carlo* sampling.

1.7.1 Gaussian Processes

Gaussian Processes (GPs) are a generalization of multivariate Gaussian distributions to the infinite dimensional case. The main use case for a GP is the description of a distribution of functions. A multivariate Gaussian distribution is defined with a *mean vector* $\boldsymbol{\mu}$ and *covariance matrix* $\boldsymbol{\sigma}$. Similarly, a GP is defined using a *mean function* $m(x)$ and a *covariance function* $k(x, y)$, also called *kernel*. The specific choice of the kernel determines the properties of the functions which make up the distribution. In particular the smoothness of the sample functions is encoded in the kernel.

With the help of Bayesian Inference, it is possible to analytically determine a GP describing the posterior distribution for a set of data points with a Gaussian likelihood and a GP prior distribution. This makes GPs a useful tool for the regression of functions with known length scales and smoothness constraints to a set of points [27]. In Chapter 5, GPs will instead be used as function generators with prescribed properties to model prior distributions.

1.7.2 Markov Chain Monte Carlo sampling

Most quantities in uncertainty quantification can be expressed as expectation values

$$\mathbb{E}[f] = \int f(\mathbf{x}) \rho(\mathbf{x}) d\mathbf{x}, \quad (1.7.4)$$

of some function $f(\mathbf{x})$ for a given probability distribution $\rho(\mathbf{x})$, which is usually the posterior distribution $p(\mathbf{x} | \mathbf{d}, \mathcal{I})$. The expectation value of \mathbf{x} is then computed with $\mathbb{E}[\mathbf{x}]$ and the variance of \mathbf{x} with $\mathbb{E}[(\mathbf{x} - \mathbb{E}[\mathbf{x}])^2]$. Similar expressions are found for other quantities which depend on \mathbf{x} . This form of *uncertainty propagation* works with an arbitrary probability distribution, in contrast to the usual Gaussian error propagation.

The integral in Equation 1.7.4 usually cannot be evaluated exactly, but can be approximated with the *sample mean*

$$\mathbb{E}[f] \approx \frac{1}{N} \sum_{i=1}^N f(\mathbf{x}_i), \quad (1.7.5)$$

where a sufficiently high number N of samples \mathbf{x}_i were drawn from the distribution $\rho(\mathbf{x})$. With the central limit theorem, it can be shown that with careful sampling, the standard error and therefore precision of this estimate, is proportional to $\frac{1}{\sqrt{N}}$, independent of the dimensions of \mathbf{x} [23].

The main difficulty when calculating expectation values in moderate to high numbers of dimensions, is that *rejection sampling* becomes very inefficient and the cumulative distribution function necessary for *inverse transform sampling* is often not available. In these cases a common approach is *Markov Chain Monte Carlo* (MCMC) sampling [33]. A *Markov Chain* is a sequence of random vectors $\{\mathbf{x}_0, \mathbf{x}_1, \dots, \mathbf{x}_t | \mathbf{x}_i \in \Xi\}$ within a state space $\Xi = \{\xi_1, \xi_2, \dots, \xi_N\}$,² where the defining property, the *Markov property*, is that the probability distribution for the t -th member of the chain \mathbf{x}_t only depends on the predecessor \mathbf{x}_{t-1} . Explicitly this can be written as

$$p(\mathbf{x}_t = \xi_j | \mathcal{I}) = \sum_{i=1}^N p(\mathbf{x}_t = \xi_j | \mathbf{x}_{t-1} = \xi_i, \mathcal{I}) p(\mathbf{x}_{t-1} = \xi_i | \mathcal{I}). \quad (1.7.6)$$

The transition probabilities from the state ξ_i to ξ_j make up the *Markov matrix* \mathbf{M} :

$$M_{ji} := p(\mathbf{x}_t = \xi_j | \mathbf{x}_{t-1} = \xi_i, \mathcal{I}). \quad (1.7.7)$$

The Markov property can be interpreted as the Markov chain having no memory, while correlations are allowed. A Markov chain should also be *homogeneous*, that is, the values of M_{ji} may not depend on the value of t . Equation 1.7.7 implies the normalization rule

$$\sum_{j=1}^N M_{ji} = 1 \quad \forall i \in \{1, \dots, N\}. \quad (1.7.8)$$

²This formalism is restricted to discrete states and while it can be generalized to continuous states, any such problem has to be discretized for numerical computations.

If the Markov chain is *irreducible*, *aperiodic* and all states are *positive recurrent*, the Markov process will converge towards an unique invariant distribution $\boldsymbol{\rho}$, for which the equation

$$\sum_{i=1}^{\mathcal{N}} M_{ji} \rho_i = \rho_j \quad \forall j \in \{1, \dots, \mathcal{N}\} \quad (1.7.9)$$

holds, independently of the initial state \mathbf{x}_0 [33]. A chain is *irreducible* if every state can be reached from any other state within a finite number of steps, i.e. there are no non-communicating regions of states. A state is positive recurrent if the expectation value of the *first return time* to the state is less than infinity. If the chain is irreducible, all states are *positive recurrent*, unless the expectation value of the first return time to the state is infinity for all states. Finally for a *periodic* state the return time may only be a multiple of some integer larger than one. A simpler sufficient, but not necessary condition for the existence of a unique stationary distribution $\boldsymbol{\rho}$ (eq. 1.7.9) is *reversibility*, i.e. that there exists a distribution $\boldsymbol{\rho}$, such that *detailed balance*

$$M_{ij} \rho_j = M_{ji} \rho_i \quad \forall i, j \in \{1, \dots, \mathcal{N}\} \quad (1.7.10)$$

is ensured. For MCMC sampling, the Markov matrix has to be constructed in such a way that the invariant distribution $\boldsymbol{\rho}$ is the target distribution [23, 33].

The approximation of expectation values with the sample mean (eq. 1.7.5) assumes *independent* samples drawn from the distribution $\boldsymbol{\rho}$. However, MCMC generates *correlated* samples. By discarding the first k samples, the correlations with the initial value are reduced and by only keeping every l -th element of the Markov chain, the correlations between the samples can be reduced. The final independent samples then contain the states $\{x_k, x_{k+l}, x_{k+2l}, \dots\}$ [33].

Metropolis-Hastings

The Metropolis-Hastings algorithm is a common way of constructing a Markov matrix for an arbitrary distribution $\boldsymbol{\rho}$. The Markov process uses the following steps repeatedly [23]:

0. The first element \mathbf{x}_0 is drawn from an initial distribution or set to a fixed starting value. The Markov chain is then $\{\mathbf{x}_0\}$.
1. To generate the next element \mathbf{x}_{t+1} for the chain $\{\mathbf{x}_0, \dots, \mathbf{x}_t\}$, first a *trial state* \mathbf{x}_p is drawn from a *proposal distribution* $q(\mathbf{x}_p | \mathbf{x}_t)$. Typically q is restricted to the vicinity of \mathbf{x}_t , resulting in a small stepsize.
2. The proposed state \mathbf{x}_p is accepted with the *acceptance probability*

$$\alpha(\mathbf{x}_p, \mathbf{x}_t) = \min \left(1, \frac{\rho(\mathbf{x}_p) q(\mathbf{x}_t | \mathbf{x}_p)}{\rho(\mathbf{x}_t) q(\mathbf{x}_p | \mathbf{x}_t)} \right). \quad (1.7.11)$$

In the case of a symmetric proposal distribution the acceptance probability simplifies to

$$\alpha(\mathbf{x}_p, \mathbf{x}_t) = \min \left(1, \frac{\rho(\mathbf{x}_p)}{\rho(\mathbf{x}_t)} \right). \quad (1.7.12)$$

3. The next element in the Markov chain is then

$$\mathbf{x}_{t+1} = \begin{cases} \mathbf{x}_p & \text{trial state accepted} \\ \mathbf{x}_t & \text{trial state rejected} \end{cases}. \quad (1.7.13)$$

Combining these steps, the Markov matrix for the Metropolis-Hastings algorithm can be written as

$$M_{ji} = q(\xi_j | \xi_i) \alpha(\xi_j | \xi_i) + \delta_{ij} \left(1 - \sum_{k=1}^{\mathcal{N}} q(\xi_k | \xi_i) \alpha(\xi_k | \xi_i) \right), \quad (1.7.14)$$

which can be proven to satisfy detailed balance (Eq. 1.7.10) [23].

The reason for restricting q to the vicinity of \mathbf{x}_t , is that the acceptance probability is ideally close to 50%, to ensure a fast and proper sampling of the target distribution. This limits the maximum stepsize unless symmetry preserving transformations, which also do not change the values of ρ , are used.

2 Grad-Shafranov equation and Solov'ev profiles

One widely investigated plasma configuration is the *tokamak*, in which the reactor and plasma ideally have *toroidal axisymmetry*, i.e. they are rotationally symmetric around a cylinder axis. Historically, tokamaks have many benefits in the design and operation of a fusion device. In this chapter, the implications of the toroidal symmetry on the MHD equations shall be elaborated. In essence the ideal MHD Equations 1.2.8-1.2.10 will be greatly simplified to a two-dimensional, non-linear, partial differential equation called the *Grad-Shafranov equation* [14, 30], which even has known analytical solutions under specific conditions.

2.1 Derivation of the Grad-Shafranov equation

2.1.1 Magnetic field

The geometry of interest can be expressed with right-handed cylinder coordinates (R, φ, Z) (see Section 1.3.1), where the toroidal axisymmetry implies that for any scalar quantity S , the toroidal derivative $\partial_\varphi S = 0$ vanishes. Writing Gauss's law for magnetism (Equation 1.2.10) in cylindrical coordinates, with physical components using the general formulation of the divergence in Equation 1.3.36, gives [13]:

$$\nabla \cdot \mathbf{B} = 0. \quad (2.1.1)$$

$$\frac{1}{R} \frac{\partial}{\partial R} (R \hat{B}_R) + \frac{\partial \hat{B}_Z}{\partial Z} + \frac{1}{R} \frac{\partial \hat{B}_\varphi}{\partial \varphi} = 0 \quad (2.1.2)$$

$$\frac{1}{R} \frac{\partial}{\partial R} (R \hat{B}_R) + \frac{\partial \hat{B}_Z}{\partial Z} = 0 \quad (2.1.3)$$

One possibility for guaranteeing this condition, is the introduction of the *magnetic vector potential* \mathbf{A} , which is related to the magnetic field with

$$\nabla \times \mathbf{A} = \mathbf{B} \quad (2.1.4)$$

and always satisfies Equation 1.2.10 as $\nabla \cdot (\nabla \times \mathbf{A}) = 0$ always holds. It is convenient to relate the toroidal component \hat{A}_φ of the vector potential with a stream function $\Psi(R, Z) = R \hat{A}_\varphi$, which can be shown to be closely related to the poloidal magnetic flux¹.

¹Note that in this chapter and for axisymmetric plasmas in general, Ψ is related to the *poloidal* magnetic flux, which is used as flux surface label. In 3D descriptions, such as in later chapters, the *toroidal* magnetic flux is denoted with ψ and used as flux surface label.

The components of the magnetic field can then be written as

$$\hat{B}_R = -\frac{1}{R} \frac{\partial \Psi}{\partial Z} \quad \text{and} \quad \hat{B}_Z = \frac{1}{R} \frac{\partial \Psi}{\partial R}. \quad (2.1.5)$$

Therefore,

$$\mathbf{B} = \hat{B}_\varphi \hat{\mathbf{e}}_\varphi + \frac{1}{R} \nabla \psi \times \hat{\mathbf{e}}_\varphi, \quad (2.1.6)$$

with a constant toroidal component \hat{B}_φ [13].

2.1.2 Current density

Inserting Equation 2.1.6 into Ampère's law (Equation 1.2.9) yields an expression for the current density \mathbf{J} , where the curl in cylinder coordinates is given in Equation 1.3.37 [13]:

$$\mu_0 \mathbf{J} = \nabla \times \mathbf{B} \quad (2.1.7)$$

$$\mu_0 \mathbf{J} = \left(\frac{1}{R} \frac{\partial \hat{B}_Z}{\partial \varphi} - \frac{\partial \hat{B}_\varphi}{\partial Z} \right) \hat{\mathbf{e}}_R + \left(\frac{\partial \hat{B}_R}{\partial Z} - \frac{\partial \hat{B}_Z}{\partial R} \right) \hat{\mathbf{e}}_\varphi + \frac{1}{R} \left(\frac{\partial (R \hat{B}_\varphi)}{\partial R} - \frac{\partial \hat{B}_R}{\partial \varphi} \right) \hat{\mathbf{e}}_Z \quad (2.1.8)$$

$$\mu_0 \mathbf{J} = \frac{1}{R} \frac{\partial (R \hat{B}_\varphi)}{\partial R} \hat{\mathbf{e}}_Z - \frac{\partial \hat{B}_\varphi}{\partial Z} \hat{\mathbf{e}}_R + \left(\frac{\partial}{\partial Z} \left(-\frac{1}{R} \frac{\partial \Psi}{\partial Z} \right) - \frac{\partial}{\partial R} \left(\frac{1}{R} \frac{\partial \Psi}{\partial R} \right) \right) \hat{\mathbf{e}}_\varphi \quad (2.1.9)$$

$$\mu_0 \mathbf{J} = \frac{1}{R} \nabla (R \hat{B}_\varphi) \times \hat{\mathbf{e}}_\varphi - \frac{1}{R} \left(\frac{\partial^2 \Psi}{\partial Z^2} + R \frac{\partial}{\partial R} \left(\frac{1}{R} \frac{\partial \Psi}{\partial R} \right) \right) \hat{\mathbf{e}}_\varphi. \quad (2.1.10)$$

The last step separates the current density into a toroidal component $\mathbf{J}_{\text{tor}} = \hat{J}_\varphi \hat{\mathbf{e}}_\varphi$ and a poloidal component $\mathbf{J}_{\text{pol}} \perp \hat{\mathbf{e}}_\varphi$:

$$\mu_0 \mathbf{J}_{\text{pol}} = \frac{1}{R} \nabla (R \hat{B}_\varphi) \times \hat{\mathbf{e}}_\varphi \quad (2.1.11)$$

$$\mu_0 \hat{J}_\varphi = -\frac{1}{R} \Delta^* \Psi, \quad (2.1.12)$$

where Δ^* is the *Grad-Shafranov operator*

$$\Delta^* \Psi := R \frac{\partial}{\partial R} \left(\frac{1}{R} \frac{\partial \Psi}{\partial R} \right) + \frac{\partial^2 \Psi}{\partial Z^2} = \hat{\mathbf{e}}_\varphi \cdot \nabla \times \nabla \times \frac{\Psi}{R} \hat{\mathbf{e}}_\varphi. \quad (2.1.13)$$

Covariant toroidal current density J_φ

Some more insight about the origin of the at first strangely looking Grad-Shafranov operator can be gained by investigating the covariant toroidal component of the current density. The orthonormal representation of the vector potential $\mathbf{A} = \frac{\Psi}{R} \hat{\mathbf{e}}_\varphi$ corresponds to a covariant representation $\mathbf{A} = \Psi \mathbf{e}^\varphi$. The covariant toroidal current density J_φ then follows from this:

$$\mathbf{B} = \nabla \times \Psi \mathbf{e}^\varphi = \frac{1}{R} \left(\frac{\partial \Psi}{\partial R} \mathbf{e}_Z - \frac{\partial \Psi}{\partial Z} \mathbf{e}_R \right) \quad (2.1.14)$$

$$\begin{aligned} \mu_0 \mathbf{J} = \nabla \times \nabla \times \Psi \mathbf{e}^\varphi &= \frac{1}{R} \left(-\frac{\partial}{\partial R} \left(\frac{1}{R} \frac{\partial \Psi}{\partial R} \right) \mathbf{e}_\varphi + \frac{1}{R} \frac{\partial^2 \Psi}{\partial \varphi \partial R} \mathbf{e}_R \right) \\ &+ \frac{1}{R} \left(\frac{1}{R} \frac{\partial^2 \Psi}{\partial \varphi \partial Z} \mathbf{e}_Z - \frac{1}{R} \frac{\partial^2 \Psi}{\partial Z^2} \mathbf{e}_\varphi \right) \end{aligned} \quad (2.1.15)$$

$$\mu_0 J^\varphi = \mathbf{e}^\varphi \cdot (\nabla \times \nabla \times \Psi \mathbf{e}^\varphi) = \frac{-1}{R^2} \left(R \frac{\partial}{\partial R} \left(\frac{1}{R} \frac{\partial \Psi}{\partial R} \right) + \frac{\partial^2 \Psi}{\partial Z^2} \right) \quad (2.1.16)$$

$$-\mu_0 J_\varphi = -\mathbf{e}_\varphi \cdot (\nabla \times \nabla \times \Psi \mathbf{e}^\varphi) = R \frac{\partial}{\partial R} \left(\frac{1}{R} \frac{\partial \Psi}{\partial R} \right) + \frac{\partial^2 \Psi}{\partial Z^2} =: \Delta^* \Psi. \quad (2.1.17)$$

In this formulation, the expression for the vector potential, the toroidal current density and the Grad-Shafranov operator take on a simpler form as the factors $\frac{1}{\mathcal{J}} = \frac{1}{R}$ have vanished.

2.1.3 Pressure p

Finally, the expressions for \mathbf{J} and \mathbf{B} are inserted into Equation 1.2.8, from which follows that ∇p is orthogonal to both \mathbf{B} and \mathbf{J} . This will be exploited by decomposing the momentum equation along \mathbf{B} and \mathbf{J} [13]:

$$\mathbf{B} \cdot \mathbf{J} \times \mathbf{B} = \mathbf{B} \cdot \nabla p \quad (2.1.18)$$

$$0 = \hat{B}_\varphi \hat{\mathbf{e}}_\varphi \cdot \frac{1}{R} \frac{\partial \mathcal{P}}{\partial \varphi} \hat{\mathbf{e}}_\varphi + \frac{1}{R} \nabla \Psi \times \hat{\mathbf{e}}_\varphi \cdot \nabla p \quad (2.1.19)$$

$$0 = \hat{\mathbf{e}}_\varphi \cdot \nabla \Psi \times \nabla p, \quad (2.1.20)$$

for which the general solution is

$$p = p(\Psi). \quad (2.1.21)$$

This confirms that the pressure is indeed a flux surface quantity. In the MHD model the pressure is a free function, usually specified from transport theory, experimental data or physical intuition.

The \mathbf{J} aligned component of Equation 1.2.8 is [13]

$$0 = \mathbf{J} \cdot \nabla p \quad (2.1.22)$$

$$0 = \frac{1}{\mu_0 R} \nabla (R \hat{B}_\varphi) \times \hat{\mathbf{e}}_\varphi \cdot \nabla p - \frac{1}{\mu_0 R} \Delta^* \Psi \hat{\mathbf{e}}_\varphi \cdot \frac{1}{R} \frac{\partial \mathcal{P}}{\partial \varphi} \hat{\mathbf{e}}_\varphi \quad (2.1.23)$$

$$0 = \hat{\mathbf{e}}_\varphi \cdot \nabla p \times \nabla (R \hat{B}_\varphi), \quad (2.1.24)$$

from which it similarly follows that $R \hat{B}_\varphi$ is a flux surface quantity and free function

$$R \hat{B}_\varphi =: F = F(p) = F(\Psi). \quad (2.1.25)$$

The same quantity already appeared in the poloidal current density

$$\mu_0 \mathbf{J}_{\text{pol}} = \frac{1}{R} \nabla F \times \hat{\mathbf{e}}_\varphi \quad (2.1.26)$$

$$\mu_0 \mathbf{J}_{\text{pol}} = \frac{1}{R} \frac{dF}{d\Psi} \nabla \Psi \times \hat{\mathbf{e}}_\varphi \quad (2.1.27)$$

and shows that the current density \mathbf{J} , just like the magnetic field \mathbf{B} , lies on surfaces of constant poloidal magnetic flux Ψ . The existence of these flux surfaces is one of the central benefits of ideal MHD equilibria. F can also be related to the poloidal current $I_{\text{pol}}(\Psi)$ enclosed within the flux surface labeled by Ψ , which is defined as

$$I_{\text{pol}}(\Psi) = \int_0^{2\pi} d\varphi \int_{r_0}^{r(\Psi)} dr R J_{\text{pol}}, \quad (2.1.28)$$

where r is the position along a radial contour orthogonal to \mathbf{J}_{pol} , r_0 is the position of the magnetic axis and the factor $R = \mathcal{J}$ is the Jacobian. Intuitively, the integration happens over any poloidal cross section from the magnetic axis to the flux surface labeled by ψ . The integral can then be solved to be

$$I_{\text{pol}}(\Psi) = 2\pi \int_{r_0}^{r(\Psi)} R \frac{1}{\mu_0 R} \frac{dF}{d\Psi} |\nabla \Psi| dr \quad (2.1.29)$$

$$I_{\text{pol}}(\Psi) = 2\pi \int_0^\Psi \frac{1}{\mu_0} \frac{dF}{d\Psi} d\Psi \quad (2.1.30)$$

$$I_{\text{pol}}(\Psi) = \frac{2\pi}{\mu_0} (F(\Psi) - F(0)). \quad (2.1.31)$$

The free function F is therefore related to the poloidal current profile with a factor and an offset equal to the magnetic field at the magnetic axis.

Using F and p , Equation 1.2.8 will be decomposed along $\nabla \Psi$ [13]:

$$\nabla \Psi \cdot \nabla p = \nabla \Psi \cdot \mathbf{J} \times \mathbf{B} \quad (2.1.32)$$

$$\nabla \Psi \cdot \nabla \Psi \frac{dp}{d\Psi} = \nabla \Psi \cdot (\mathbf{J}_{\text{pol}} \times \mathbf{B}_{\text{tor}} + \mathbf{J}_{\text{tor}} \times \mathbf{B}_{\text{pol}}) \quad (2.1.33)$$

$$(\nabla \Psi)^2 \frac{dp}{d\Psi} = \nabla \Psi \cdot \left(\left(\frac{1}{\mu_0 R} \frac{dF}{d\Psi} \nabla \Psi \times \hat{\mathbf{e}}_\varphi \right) \times \hat{B}_\varphi \hat{\mathbf{e}}_\varphi + \hat{J}_\varphi \hat{\mathbf{e}}_\varphi \times \left(\frac{1}{R} \nabla \Psi \times \hat{\mathbf{e}}_\varphi \right) \right) \quad (2.1.34)$$

$$(\nabla \Psi)^2 \frac{dp}{d\Psi} = \left(\frac{1}{\mu_0 R} \frac{dF}{d\Psi} \hat{B}_\varphi - \hat{J}_\varphi \frac{1}{R} \right) \nabla \Psi \cdot (\nabla \Psi \times \hat{\mathbf{e}}_\varphi) \times \hat{\mathbf{e}}_\varphi. \quad (2.1.35)$$

At this point, the vector part simplifies to

$$\nabla \Psi \cdot (\nabla \Psi \times \hat{\mathbf{e}}_\varphi) \times \hat{\mathbf{e}}_\varphi = \nabla \Psi \cdot (\hat{\mathbf{e}}_\varphi (\nabla \Psi \cdot \hat{\mathbf{e}}_\varphi) - \nabla \Psi (\hat{\mathbf{e}}_\varphi \cdot \hat{\mathbf{e}}_\varphi)) \quad (2.1.36)$$

$$\nabla \Psi \cdot (\nabla \Psi \times \hat{\mathbf{e}}_\varphi) \times \hat{\mathbf{e}}_\varphi = -(\nabla \Psi)^2. \quad (2.1.37)$$

Inserting this back into Equation 2.1.35 results in a scalar differential equation, which is further simplified by inserting Equations 2.1.12 and 2.1.25 for \hat{B}_φ and \hat{J}_φ :

$$(\nabla\Psi)^2 \frac{dp}{d\Psi} = -(\nabla\Psi)^2 \left(\frac{1}{\mu_0 R} \frac{dF}{d\Psi} B_\varphi - \frac{1}{R} J_\varphi \right) \quad (2.1.38)$$

$$\frac{dp}{d\Psi} = -\frac{1}{\mu_0 R} \frac{dF}{d\Psi} \frac{F}{R} - \frac{1}{\mu_0 R^2} \Delta^* \Psi. \quad (2.1.39)$$

The last step requires that the gradient $\nabla\Psi$ does not vanish. It can however be shown, that there exist no toroidally axisymmetric MHD equilibria where the gradient of the poloidal magnetic flux and therefore $\nabla\Psi$ vanishes [13]. Equation 2.1.39 finally leads to the *Grad-Shafranov equation* [14, 30]

$$\Delta^* \Psi := R \frac{\partial}{\partial R} \left(\frac{1}{R} \frac{\partial \Psi}{\partial R} \right) + \frac{\partial^2 \Psi}{\partial Z^2} = -\mu_0 R^2 \frac{dp}{d\Psi} - \frac{1}{2} \frac{dF^2}{d\Psi}. \quad (2.1.40)$$

The three coupled three-dimensional static MHD equations have now been reduced to a single two-dimensional, non-linear, partial differential equation. In most cases there are no known analytical solutions, but the Grad-Shafranov equation is significantly easier to solve than the static MHD equations, to the point that several numerical Grad-Shafranov solvers exist, which can provide solutions very quickly.

2.2 Analytical solutions for Solov'ev profiles

The *Solov'ev profiles* [4, 32] are specific forms of $F^2(\Psi)$ and $p(\Psi)$ for which analytical solutions to the Grad-Shafranov equation are known. In particular the Solov'ev profiles are linear in Ψ and given as

$$F \frac{dF}{d\Psi} = \frac{1}{2} \frac{dF^2}{d\Psi} = -A \quad \text{and} \quad \mu_0 \frac{dp}{d\Psi} = -C, \quad (2.2.1)$$

such that the constants A and C fully specify the two profiles. The constant offset of both profiles is irrelevant to the physics, but determined by boundary conditions, i.e. magnetic field at the axis and the pressure at the plasma boundary. As $F^2(\Psi)$ is linear in Ψ , the poloidal current $I_{\text{pol}}(\Psi)$ has a square root profile. The Grad-Shafranov equation (2.1.40) becomes

$$\Delta^* \Psi := R \frac{\partial}{\partial R} \left(\frac{1}{R} \frac{\partial \Psi}{\partial R} \right) + \frac{\partial^2 \Psi}{\partial Z^2} = A - C R^2. \quad (2.2.2)$$

With the further renormalization $R = R_0 x$, $Z = R_0 y$, $\Psi = \Psi_0 u$ and $\alpha = \frac{A R_0^2}{\Psi_0}$, where $\Psi_0 = R_0^2(A + C R_0^2)$, it simplifies to

$$x \frac{\partial}{\partial x} \left(\frac{1}{x} \frac{\partial u}{\partial x} \right) + \frac{\partial^2 u}{\partial y^2} = \alpha + (1 - \alpha) x^2. \quad (2.2.3)$$

Effectively the renormalization was chosen such that all quantities become dimensionless and α and Ψ_0 are now the two parameters defining the profiles. This has the advantage that the differential equation now only depends on α and Ψ_0 is an independent scale factor.

2.2.1 Particular and homogeneous solutions

The particular solution to Equation 2.2.3 is [4]

$$u_0(x, y) = \frac{\alpha}{2}x^2 \ln x + \frac{1-\alpha}{8}x^4. \quad (2.2.4)$$

The homogeneous solutions can be expressed as simple basis functions which solve $\Delta^* u = 0$ and match the desired boundary. Cerfon and Freidberg [4] suggest that the boundary is described with a number of pointwise constraints equal to the finite number of basis functions. In this way the solution space is reduced, but the resulting system of equations can be solved quickly and the desired shapes can be easily specified. For top-down symmetric configurations they suggest the basis functions [4, 9]:

$$u_1(x, y) = 1, \quad (2.2.5)$$

$$u_2(x, y) = x^2, \quad (2.2.6)$$

$$u_3(x, y) = y^2 - x^2 \ln x, \quad (2.2.7)$$

$$u_4(x, y) = x^4 - 4x^2 y^2, \quad (2.2.8)$$

$$u_5(x, y) = 2y^4 - 9y^2 x^2 - (12y^2 x^2 - 3x^4) \ln x, \quad (2.2.9)$$

$$u_6(x, y) = x^6 - 12x^4 y^2 + 8x^2 y^4 \quad (2.2.10)$$

$$\text{and } u_7(x, y) = 8y^6 - 140y^4 x^2 + 75y^2 x^4 \\ - (120y^4 x^2 - 180y^2 x^4 + 15x^6) \ln x. \quad (2.2.11)$$

For asymmetric configurations additional basis functions with odd powers of y are required:

$$u_8(x, y) = y, \quad (2.2.12)$$

$$u_9(x, y) = yx^2, \quad (2.2.13)$$

$$u_{10}(x, y) = y^3 - 3yx^2 \ln x, \quad (2.2.14)$$

$$u_{11}(x, y) = 4y^3 x^2 - 3yx^4 \quad (2.2.15)$$

$$\text{and } u_{12}(x, y) = 8y^5 - 45yx^4 - (80y^3 x^2 - 60yx^4) \ln x. \quad (2.2.16)$$

2.2.2 Boundary constraints

The plasma boundary is specified with 7 or 12 constraints for top-down symmetric and asymmetric plasmas. These conditions are related to a number of parameters, which describe the shape of typical toroidal cross sections. This reference surface is given parametrically in terms of the 2π periodic parameter τ as [13]

$$\begin{pmatrix} X \\ Y \end{pmatrix} = \begin{pmatrix} 1 + \epsilon \cos(\tau + \delta_0 \sin \tau) \\ \epsilon \kappa \sin \tau \end{pmatrix}, \quad (2.2.17)$$

where ϵ is the *inverse aspect ratio*, κ the *elongation* and $\delta = \sin \delta_0$ the *triangularity*. The boundary conditions are then the properties of the reference surface at three specific points:

the *outer equatorial point* at $\mathbf{x}_o = (1 + \epsilon, 0)$, the *inner equatorial point* at $\mathbf{x}_i = (1 - \epsilon, 0)$ and the *high point* at $\mathbf{x}_h = (1 - \delta\epsilon, \kappa\epsilon)$. The 7 conditions are:

$$u(\mathbf{x}_o) = 0 \quad \text{outer point flux,} \quad (2.2.18)$$

$$\frac{\partial^2 u}{\partial y^2}(\mathbf{x}_o) = -\frac{(1 + \delta_0)^2}{\epsilon \kappa^2} \frac{\partial u}{\partial x}(\mathbf{x}_o) \quad \text{outer point curvature,} \quad (2.2.19)$$

$$u(\mathbf{x}_i) = 0 \quad \text{inner point flux,} \quad (2.2.20)$$

$$\frac{\partial^2 u}{\partial y^2}(\mathbf{x}_i) = \frac{(1 - \delta_0)^2}{\epsilon \kappa^2} \frac{\partial u}{\partial x}(\mathbf{x}_i) \quad \text{inner point curvature,} \quad (2.2.21)$$

$$u(\mathbf{x}_h) = 0 \quad \text{high point flux,} \quad (2.2.22)$$

$$\frac{\partial u}{\partial x}(\mathbf{x}_h) = 0 \quad \text{high point slope} \quad (2.2.23)$$

$$\text{and } \frac{\partial^2 u}{\partial x^2}(\mathbf{x}_h) = \frac{\kappa}{\epsilon \cos^2(\delta_0)} \frac{\partial u}{\partial y}(\mathbf{x}_h) \quad \text{high point curvature.} \quad (2.2.24)$$

Many modern tokamaks have a top-down asymmetric configuration with a divertor instead of plasma limiters. The defining change in the flux surface geometry is the existence of the *seperatrix* with the *X-point*. This is a saddle point in the flux Ψ , which can also be thought of as the intersection of two flux surfaces corresponding to the same flux. The divertor configuration has been instrumental in increasing the magnetic confinement in tokamaks. An up-down asymmetric configuration with an X-point is built with the additional five basis functions with odd powers of y and therefore needs five additional constraints. The first two are the slope conditions at the inner and outer equatorial points, which were fulfilled automatically in the up-down symmetric case. The three remaining constraints are that the flux and both of its derivatives, corresponding to the poloidal magnetic field, need to vanish at the X-point located at $\mathbf{x}_{sep} = (x_{sep}, y_{sep})$, where $y_{sep} < 0$. Formally the five extra constraints are [4]:

$$\frac{\partial u}{\partial y}(\mathbf{x}_o) = 0 \quad \text{outer point slope,} \quad (2.2.25)$$

$$\frac{\partial u}{\partial y}(\mathbf{x}_i) = 0 \quad \text{inner point slope,} \quad (2.2.26)$$

$$u(\mathbf{x}_{sep}) = 0 \quad \text{X-point flux,} \quad (2.2.27)$$

$$\frac{\partial u}{\partial x}(\mathbf{x}_{sep}) = 0 \quad \text{X-point } B_y = 0 \quad (2.2.28)$$

$$\text{and } \frac{\partial u}{\partial y}(\mathbf{x}_{sep}) = 0 \quad \text{X-point } B_x = 0. \quad (2.2.29)$$

Finally, there is also the possibility to have a top-down symmetric configuration with two X-points. In this case the seven symmetric basis functions are enough. The conditions 2.2.22 to 2.2.24 however need to be modified as the X-point at $\mathbf{x}_{sep} = (x_{sep}, y_{sep})$ is the new high point. Just like in the asymmetric case, the flux and both its derivatives need

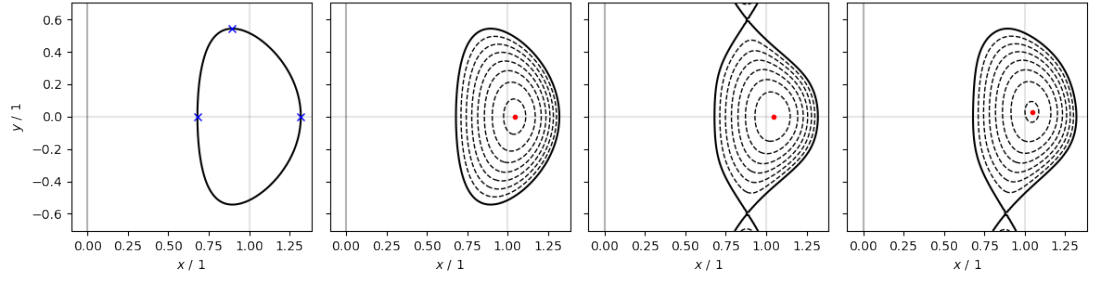


Figure 2.1: The reference surface for the poloidal cross section of the plasma boundary, with the outer and inner equatorial points as well as the high point marked, alongside the surfaces of constant flux Ψ for MHD equilibria with top-down symmetry and no X-points, two X-points and a non-symmetric equilibrium with a single X-point.

to vanish at the X-point. Formally the new constraints are [4]:

$$u(\mathbf{x}_{sep}) = 0 \quad \text{X-point flux,} \quad (2.2.30)$$

$$\frac{\partial u}{\partial x}(\mathbf{x}_{sep}) = 0 \quad \text{X-point } B_y = 0 \quad (2.2.31)$$

$$\text{and } \frac{\partial u}{\partial y}(\mathbf{x}_{sep}) = 0 \quad \text{X-point } B_x = 0. \quad (2.2.32)$$

Figure 2.1 shows a comparison of the reference surface and poloidal cuts of the three possible configurations. They all use the same shape factors $\epsilon = 0.32$, $\kappa = 1.7$ and $\delta = 0.33$. The two divertor configurations use the X-point at $\mathbf{x}_{sep} = (1 - 1.1\delta\epsilon, -1.1\kappa\epsilon)$.

3 Radial force balance and consistent profiles

Starting from the MHD equilibrium Equations 1.2.8 to 1.2.10, in this chapter a weak formulation of the force balance, called the *radial force balance* is derived for a 3D MHD equilibrium defined by the inverse coordinate mapping, e.g. as calculated by VMEC (Section 1.5).

3.1 Derivation of the radial force balance

The fundamental idea of the radial force balance is to compute the flux surface average $\langle\langle \mathbf{F} \rangle\rangle$ of the local force balance

$$\mathbf{F} = \mathbf{J} \times \mathbf{B} - \nabla p. \quad (3.1.1)$$

The first step is to decompose the local force balance in the right-handed flux coordinates (ρ, ϑ, ζ) (Section 1.4.1):

$$\mathbf{F} = (J^\rho \mathbf{e}_\rho + J^\vartheta \mathbf{e}_\vartheta + J^\zeta \mathbf{e}_\zeta) \times (\cancel{B^\rho \mathbf{e}_\rho} + B^\vartheta \mathbf{e}_\vartheta + B^\zeta \mathbf{e}_\zeta) - \frac{dp}{d\rho} \nabla \rho \quad (3.1.2)$$

$$\mathbf{F} = J^\rho B^\vartheta \mathbf{e}_\rho \times \mathbf{e}_\vartheta + (J^\vartheta B^\zeta - J^\zeta B^\vartheta) \mathbf{e}_\vartheta \times \mathbf{e}_\zeta - J^\rho B^\zeta \mathbf{e}_\zeta \times \mathbf{e}_\rho - \frac{dp}{d\rho} \mathbf{e}^\rho \quad (3.1.3)$$

$$F_\rho = \mathcal{J} (J^\vartheta B^\zeta - J^\zeta B^\vartheta) - \frac{dp}{d\rho} \quad (3.1.4)$$

$$F_\vartheta = -\mathcal{J} J^\rho B^\zeta \quad (3.1.5)$$

$$F_\zeta = \mathcal{J} J^\rho B^\vartheta, \quad (3.1.6)$$

where B^ρ vanishes, as the magnetic field lines lie on the flux surfaces. Expanding Equation 1.4.7 with the inter-relationship between co- and contravariant components given by Equation 1.3.10 and the definition of the rotational transform ι in Equation 1.5.1, the magnetic field \mathbf{B} becomes:

$$\mathbf{B} = \nabla \psi \times \nabla \vartheta^* + \nabla \zeta \times \nabla \chi \quad (3.1.7)$$

$$\mathbf{B} = \frac{d\psi}{d\rho} \nabla \rho \times \nabla (\vartheta + \lambda) + \frac{d\chi}{d\rho} \nabla \zeta \times \nabla \rho \quad (3.1.8)$$

$$\mathbf{B} = \frac{d\psi}{d\rho} \nabla \rho \times \left(\nabla \vartheta + \frac{\partial \lambda}{\partial \vartheta} \nabla \vartheta + \frac{\partial \lambda}{\partial \zeta} \nabla \zeta \right) + \iota \frac{d\psi}{d\rho} \nabla \zeta \times \nabla \rho \quad (3.1.9)$$

$$\mathbf{B} = \frac{1}{\mathcal{J}} \frac{d\psi}{d\rho} \left(1 + \frac{\partial \lambda}{\partial \vartheta} \right) \mathbf{e}_\zeta + \frac{1}{\mathcal{J}} \frac{d\psi}{d\rho} \left(\iota - \frac{\partial \lambda}{\partial \zeta} \right) \mathbf{e}_\vartheta. \quad (3.1.10)$$

Therefore the contravariant components of the magnetic field are

$$B^\rho = 0, \quad (3.1.11)$$

$$B^\vartheta = \frac{1}{\mathcal{J}} \frac{d\psi}{d\rho} \left(\iota - \frac{\partial\lambda}{\partial\zeta} \right) \quad (3.1.12)$$

$$\text{and } B^\zeta = \frac{1}{\mathcal{J}} \frac{d\psi}{d\rho} \left(1 + \frac{\partial\lambda}{\partial\vartheta} \right), \quad (3.1.13)$$

which can be transformed to covariant components using Equation 1.3.17:

$$B_\alpha = g_{\alpha\vartheta} B^\vartheta + g_{\alpha\zeta} B^\zeta \quad (3.1.14)$$

$$B_\alpha = \frac{1}{\mathcal{J}} \frac{d\psi}{d\rho} \left(g_{\alpha\vartheta} \left(\iota - \frac{\partial\lambda}{\partial\zeta} \right) + g_{\alpha\zeta} \left(1 + \frac{\partial\lambda}{\partial\vartheta} \right) \right), \quad (3.1.15)$$

where $\alpha \in \{\rho, \vartheta, \zeta\}$.

The current density \mathbf{J} is defined by Equation 1.2.9 and the curl in curvilinear coordinates for covariant components is given in Equation 1.3.26. Combined, the contravariant components of \mathbf{J} are then:

$$J^\rho = \frac{1}{\mu_0 \mathcal{J}} \left(\frac{\partial B_\zeta}{\partial\vartheta} - \frac{\partial B_\vartheta}{\partial\zeta} \right) \stackrel{!}{=} 0, \quad (3.1.16)$$

$$J^\vartheta = \frac{1}{\mu_0 \mathcal{J}} \left(\frac{\partial B_\rho}{\partial\zeta} - \frac{\partial B_\zeta}{\partial\rho} \right) \quad (3.1.17)$$

$$\text{and } J^\zeta = \frac{1}{\mu_0 \mathcal{J}} \left(\frac{\partial B_\vartheta}{\partial\rho} - \frac{\partial B_\rho}{\partial\vartheta} \right), \quad (3.1.18)$$

where $J^\rho \stackrel{!}{=} 0$ if the force balance $F_\vartheta = 0$ and $F_\zeta = 0$ (Equations 3.1.5 and 3.1.6) should be fulfilled.

Inserting these terms into Equation 3.1.4 gives

$$F_\rho = \frac{1}{\mu_0 \mathcal{J}} \frac{d\psi}{d\rho} \left(\left(\frac{\partial B_\rho}{\partial\zeta} - \frac{\partial B_\zeta}{\partial\rho} \right) \left(1 + \frac{\partial\lambda}{\partial\vartheta} \right) - \left(\frac{\partial B_\vartheta}{\partial\rho} - \frac{\partial B_\rho}{\partial\vartheta} \right) \left(\iota - \frac{\partial\lambda}{\partial\zeta} \right) \right) - \frac{dp}{d\rho}. \quad (3.1.19)$$

The quantity of interest is the flux surface averaged radial force, defined by

$$\langle\langle F_\rho \rangle\rangle(\rho) := \frac{\langle \mathcal{J} F_\rho \rangle}{\langle \mathcal{J} \rangle} := \frac{\iint d\vartheta d\zeta \mathcal{J} F_\rho}{\iint d\vartheta d\zeta \mathcal{J}}, \quad (3.1.20)$$

as the differential volume element $dV = \mathcal{J} d\rho d\vartheta d\zeta$ [6]. All the components of \mathbf{B} , as well as λ are continuous and therefore periodic in ϑ and ζ . For any such function it follows that

$$\left\langle \frac{\partial f}{\partial\vartheta} \right\rangle = \int_0^{2\pi} d\vartheta \int_0^{2\pi} d\zeta \frac{\partial f}{\partial\zeta} = \int_0^{2\pi} d\vartheta f \Big|_0^{2\pi} = 0 \quad (3.1.21)$$

$$\left\langle f \frac{\partial\lambda}{\partial\vartheta} \right\rangle = \int_0^{2\pi} d\zeta f \lambda \Big|_0^{2\pi} - \left\langle \frac{\partial f}{\partial\vartheta} \lambda \right\rangle = - \left\langle \frac{\partial f}{\partial\vartheta} \lambda \right\rangle, \quad (3.1.22)$$

and likewise

$$\left\langle \frac{\partial f}{\partial \zeta} \right\rangle = 0 \quad (3.1.23)$$

$$\left\langle f \frac{\partial \lambda}{\partial \zeta} \right\rangle = - \left\langle \frac{\partial f}{\partial \zeta} \lambda \right\rangle. \quad (3.1.24)$$

With these relations, the terms in Equation 3.1.19 simplify to

$$\left\langle \frac{\partial B_\rho}{\partial \zeta} \right\rangle = 0, \quad (3.1.25)$$

$$\left\langle \frac{\partial B_\rho}{\partial \vartheta} \iota \right\rangle = 0, \quad (3.1.26)$$

$$\left\langle \frac{\partial B_\rho}{\partial \zeta} \frac{\partial \lambda}{\partial \vartheta} - \frac{\partial B_\rho}{\partial \vartheta} \frac{\partial \lambda}{\partial \zeta} \right\rangle = \left\langle -\frac{\partial^2 B_\rho}{\partial \zeta \partial \vartheta} \lambda + \frac{\partial^2 B_\rho}{\partial \vartheta \partial \zeta} \lambda \right\rangle = 0 \quad (3.1.27)$$

$$\text{and } \left\langle -\frac{\partial B_\zeta}{\partial \rho} \frac{\partial \lambda}{\partial \vartheta} + \frac{\partial B_\vartheta}{\partial \rho} \frac{\partial \lambda}{\partial \zeta} \right\rangle = \left\langle \frac{\partial B_\zeta}{\partial \rho \partial \vartheta} \lambda - \frac{\partial B_\vartheta}{\partial \rho \partial \zeta} \lambda \right\rangle = \left\langle \mu_0 \frac{\partial \mathcal{J}_\vartheta J^\rho}{\partial \rho} \lambda \right\rangle \stackrel{!}{=} 0. \quad (3.1.28)$$

Additionally, inverting the definition of ρ (Section 1.4) gives

$$\psi(\rho) = \psi_0 \rho^2 \quad (3.1.29)$$

$$\text{and } \frac{d\psi}{d\rho} = 2\rho\psi_0. \quad (3.1.30)$$

Equation 3.1.20 therefore becomes the *radial force balance*:

$$\langle\langle F_\rho \rangle\rangle(\rho) = \frac{-2\rho\psi_0}{\mu_0 \langle \mathcal{J} \rangle} \left(\frac{\partial}{\partial \rho} \langle B_\zeta \rangle + \iota \frac{\partial}{\partial \rho} \langle B_\vartheta \rangle \right) - \frac{dp}{d\rho}. \quad (3.1.31)$$

With this equation, the *consistent pressure gradient* $\frac{dp}{d\rho}$ can also be computed from the magnetic field, defined by the flux surface geometry, under the assumption that $\langle\langle F_\rho \rangle\rangle = 0$ must be fulfilled:

$$\frac{dp}{d\rho} = \frac{-2\rho\psi_0}{\mu_0 \langle \mathcal{J} \rangle} \left(\frac{\partial}{\partial \rho} \langle B_\zeta \rangle + \iota \frac{\partial}{\partial \rho} \langle B_\vartheta \rangle \right). \quad (3.1.32)$$

3.2 Toroidal and poloidal current profiles

Two other quantities of interest are the toroidal and poloidal current profiles $I_{\text{tor}}(\rho)$ and $I_{\text{pol}}(\rho)$. They can be calculated by integrating the current density \mathbf{J} over surfaces of constant ζ and ϑ from the magnetic axis up to a flux surface ρ . For the toroidal current this is

$$I_{\text{tor}}(\tilde{\rho}) = \int_{\partial\zeta(\tilde{\rho})} d\mathbf{x}_\zeta \cdot \mathbf{J}, \quad (3.2.1)$$

where $d\mathbf{x}_\zeta$ is the surface normal vector

$$d\mathbf{x}_\zeta = d\rho d\vartheta \frac{d\mathbf{x}}{d\rho} \times \frac{d\mathbf{x}}{d\vartheta}. \quad (3.2.2)$$

It follows that

$$I_{\text{tor}}(\tilde{\rho}) = \int_0^{\tilde{\rho}} d\rho \int d\vartheta \frac{d\mathbf{x}}{d\rho} \times \frac{d\mathbf{x}}{d\vartheta} \cdot \mathbf{J} \quad (3.2.3)$$

$$I_{\text{tor}}(\tilde{\rho}) = \int_0^{\tilde{\rho}} d\rho \int d\vartheta \mathcal{J} \mathbf{e}^\zeta \cdot \mathbf{J} \quad (3.2.4)$$

$$I_{\text{tor}}(\tilde{\rho}) = \int_0^{\tilde{\rho}} d\rho \int d\vartheta \mathcal{J} J^\zeta \quad (3.2.5)$$

and likewise

$$I_{\text{pol}}(\tilde{\rho}) = \int_{\partial\vartheta(\tilde{\rho})} d\mathbf{x}_\vartheta \cdot \mathbf{J} \quad (3.2.6)$$

$$I_{\text{pol}}(\tilde{\rho}) = \int_0^{\tilde{\rho}} d\rho \int d\zeta \mathcal{J} J^\vartheta. \quad (3.2.7)$$

By inserting the Equations 3.1.17 and 3.1.18, the integrals become

$$I_{\text{tor}}(\tilde{\rho}) = \frac{1}{\mu_0} \int_0^{\tilde{\rho}} d\rho \int_0^{2\pi} d\vartheta \mathcal{J} \frac{1}{\mathcal{J}} \left(\frac{\partial B_\vartheta}{\partial \rho} - \frac{\partial B_\rho}{\partial \vartheta} \right) \quad (3.2.8)$$

$$I_{\text{tor}}(\tilde{\rho}) = \frac{1}{\mu_0} \int_0^{2\pi} d\vartheta B_\vartheta \Big|_{\rho=0}^{\tilde{\rho}} - \cancel{\frac{1}{\mu_0} \int_0^{\tilde{\rho}} d\rho B_\rho \Big|_{\vartheta=0}^{2\pi}} \quad (3.2.9)$$

$$I_{\text{tor}}(\tilde{\rho}) = \frac{1}{2\pi\mu_0} \int_0^{2\pi} d\vartheta \int_0^{2\pi} d\zeta B_\vartheta(\tilde{\rho}) \quad (3.2.10)$$

$$I_{\text{tor}}(\tilde{\rho}) = \frac{1}{2\pi\mu_0} \langle B_\vartheta \rangle(\tilde{\rho}) \quad (3.2.11)$$

where $B_\vartheta = 0$ has to vanish at the magnetic axis ($\rho = 0$) and

$$I_{\text{pol}}(\tilde{\rho}) = \frac{1}{\mu_0} \int_0^{\tilde{\rho}} d\rho \int_0^{2\pi} d\zeta \mathcal{J} \frac{1}{\mathcal{J}} \left(\frac{\partial B_\rho}{\partial \zeta} - \frac{\partial B_\zeta}{\partial \rho} \right) \quad (3.2.12)$$

$$I_{\text{pol}}(\tilde{\rho}) = \cancel{\frac{1}{\mu_0} \int_0^{\tilde{\rho}} d\rho B_\rho \Big|_{\zeta=0}^{2\pi}} - \frac{1}{\mu_0} \int_0^{2\pi} d\zeta B_\zeta \Big|_{\rho=0}^{\tilde{\rho}} \quad (3.2.13)$$

$$I_{\text{pol}}(\tilde{\rho}) = \frac{-1}{2\pi\mu_0} \int_0^{2\pi} d\vartheta \int_0^{2\pi} d\zeta B_\zeta \Big|_{\rho=0}^{\tilde{\rho}} \quad (3.2.14)$$

$$I_{\text{pol}}(\tilde{\rho}) = \frac{1}{2\pi\mu_0} (\langle B_\zeta \rangle(0) - \langle B_\zeta \rangle(\tilde{\rho})). \quad (3.2.15)$$

Because the toroidal magnetic field at the magnetic axis is not always known, another quantity of interest is the *partial poloidal current*

$$\tilde{I}_{\text{pol}}(\rho) = \frac{-1}{2\pi\mu_0} \langle B_\zeta \rangle(\rho), \quad (3.2.16)$$

where crucially

$$\frac{dI_{\text{pol}}}{d\rho} = \frac{d\tilde{I}_{\text{pol}}}{d\rho} \quad (3.2.17)$$

holds.

With these two formulas, the radial force balance (Equation 3.1.31) can also be rewritten in terms of the currents as

$$\langle\langle F_\rho \rangle\rangle(\rho) = \frac{4\rho\pi\psi_0}{\langle\mathcal{J}\rangle} \left(\frac{dI_{\text{pol}}}{d\rho} - \iota \frac{dI_{\text{tor}}}{d\rho} \right) - \frac{dp}{d\rho} \quad (3.2.18)$$

and with the toroidal and poloidal flux explicitly as

$$\langle\langle F_\rho \rangle\rangle(\rho) = \frac{2\pi}{\langle\mathcal{J}\rangle} \left(\frac{d\psi}{d\rho} \frac{dI_{\text{pol}}}{d\rho} - \frac{d\chi}{d\rho} \frac{dI_{\text{tor}}}{d\rho} \right) - \frac{dp}{d\rho}. \quad (3.2.19)$$

Similarly the consistent pressure gradient can be computed with

$$\frac{dp}{d\rho} = \frac{4\pi\rho\psi_0}{\langle\mathcal{J}\rangle} \left(\frac{dI_{\text{pol}}}{d\rho} - \iota \frac{dI_{\text{tor}}}{d\rho} \right). \quad (3.2.20)$$

3.3 Numerical implementation

While the VMEC representation of an MHD equilibrium (Sections 1.4.1 and 1.5) uses a Fourier basis for the toroidal and poloidal directions, the radial direction is specified with discrete, equidistant flux surfaces and a finite difference scheme is used to compute the derivatives. In particular, the radial coordinate ρ is discretized with K points such that the *full mesh* consists of the points

$$\rho_k = \sqrt{\frac{k}{K-1}} \quad k \in \{0, 1, \dots, K-1\}. \quad (3.3.1)$$

This is equivalent to an equidistant grid in the normalized toroidal flux $s = \rho^2 \propto \psi$. In order to increase the accuracy of the finite difference derivatives, a *half mesh*

$$\bar{\rho}_k = \sqrt{\frac{2k-1}{2K-2}} = \sqrt{\frac{\rho_{k-1}^2 + \rho_k^2}{2}} \quad k \in \{1, \dots, K-1\} \quad (3.3.2)$$

is defined additionally¹. A quantity $f(\rho)$ defined on the full mesh with the values f_k at the positions ρ_k can be linearly interpolated to the half mesh values \bar{f}_k at the positions $\bar{\rho}_k$ with

$$\bar{f}_k = \frac{f_{k-1} + f_k}{2}. \quad (3.3.3)$$

The derivative $\frac{df}{d\rho}$ at the half mesh positions $\bar{\rho}_k$, for f defined on the full mesh is a first order finite difference in the normalized flux ρ^2 and therefore

$$\frac{df}{d\rho}(\bar{\rho}_k) = 2\bar{\rho}_k \frac{f_k - f_{k-1}}{K-1}. \quad (3.3.4)$$

¹Half mesh quantities will be denoted with a bar, e.g. $\bar{f}_k = f(\bar{\rho}_k)$, to differentiate them from the full mesh quantities $f_k = f(\rho_k)$.

Similarly, differentiating a half mesh quantity yields

$$\frac{\partial f}{\partial \rho}(\rho_k) = 2\rho_k \frac{\bar{f}_k - \bar{f}_{k+1}}{K-1}. \quad (3.3.5)$$

The third possibility for the first derivative is the second order central difference, where the derivative is evaluated on the same mesh as the quantity. It is defined as

$$\frac{\partial f}{\partial \rho}(\rho_k) = 2\rho_k \frac{f_{k+1} - f_{k-1}}{2(K-1)}.$$

In addition to the radial derivatives, the angular derivatives of R, Z and λ will also be required. As R, Z and λ are defined as Fourier series (Equations 1.5.2 to 1.5.4) the derivatives are:

$$\frac{\partial R}{\partial \vartheta}(\rho_k) = \sum_{m=0}^M \sum_{n=-N}^N (-m) R_{kmn} \sin(m\vartheta - nN_{FP}\zeta), \quad (3.3.6)$$

$$\frac{\partial R}{\partial \zeta}(\rho_k) = \sum_{m=0}^M \sum_{n=-N}^N n N_{FP} R_{kmn} \sin(m\vartheta - nN_{FP}\zeta), \quad (3.3.7)$$

$$\frac{\partial Z}{\partial \vartheta}(\rho_k) = \sum_{m=0}^M \sum_{n=-N}^N m Z_{kmn} \cos(m\vartheta - nN_{FP}\zeta), \quad (3.3.8)$$

$$\frac{\partial Z}{\partial \zeta}(\rho_k) = \sum_{m=0}^M \sum_{n=-N}^N (-nN_{FP}) Z_{kmn} \cos(m\vartheta - nN_{FP}\zeta), \quad (3.3.9)$$

$$\frac{\partial \lambda}{\partial \vartheta}(\bar{\rho}_k) = \sum_{m=0}^M \sum_{n=-N}^N m \bar{\lambda}_{kmn} \cos(m\vartheta - nN_{FP}\zeta) \quad (3.3.10)$$

$$\text{and } \frac{\partial \lambda}{\partial \zeta}(\bar{\rho}_k) = \sum_{m=0}^M \sum_{n=-N}^N (-nN_{FP}) \bar{\lambda}_{kmn} \cos(m\vartheta - nN_{FP}\zeta). \quad (3.3.11)$$

With this, all the ingredients for the calculation of the consistent pressure gradient (Equation 3.1.32) and the toroidal and poloidal currents (Equations 3.2.11 and 3.2.15) are available. The magnetic field turns out to be a half mesh quantity, while the current density and pressure gradient are defined on the full mesh. The R and Z coordinate, as well as the ι profile will be required on both meshes, the former in particular to calculate \mathcal{J} and g_{ij} . The integration of the magnetic field $\langle B_\vartheta \rangle$ and $\langle B_\zeta \rangle$ over a flux surface can be calculated using a grid in ϑ and ζ . The convergence of this integration with respect to the chosen resolution is investigated in Section 4.4.4.

4 Describing MHD equilibrium distributions

The central part of the presented work is the description of low dimensional 3D MHD equilibrium distributions. Such distributions might be prior or posterior probability distributions for MHD equilibrium reconstruction (Chapter 5) or more generally describe any related family of equilibria. The low dimensional representation would allow drawing samples from this distribution, e.g to perform Bayesian Inference or uncertainty quantification with an MCMC approach. Such a non-intrusive uncertainty quantification could be done with any simulation, which takes an MHD equilibrium as input and the comparatively low dimensionality would significantly reduce the required number of samples.

4.1 Equilibrium defining parameters

3D MHD solvers like VMEC [15] (Sections 1.4.1 and 1.5) or DESC [7] typically solve for the inverse coordinate transform. That is, they solve for the real space positions of the flux surfaces, which define the magnetic field through magnetic flux coordinates (Section 1.4), rather than solving for the flux as a function of the real space coordinates as in Chapter 2. VMEC describes the flux surfaces with $R(\rho, \vartheta, \zeta)$, $Z(\rho, \vartheta, \zeta)$ and $\lambda(\rho, \vartheta, \zeta)$ ¹ and additionally needs ψ_0 , $\iota(\rho)$ and N_{FP} to fully describe an MHD equilibrium. In VMEC, R , Z and λ are Fourier series in ϑ and ζ , which in the case of *stellarator symmetry* reduce to pure cosine or sine series. ρ is discretized on a grid, which in total means that a VMEC equilibrium is described by the Fourier modes R_{kmn} , Z_{kmn} and $\bar{\lambda}_{lmn}$, as well as the profile values ι_k for each full mesh position ρ_k or half mesh position $\bar{\rho}_l$. ψ_0 is an additional scalar parameter while N_{FP} is constant. From the five base quantities and N_{FP} , all other equilibrium quantities can be computed. For example, Equation 3.1.32 can be used to calculate the *consistent pressure profile* $\frac{dp}{d\rho}$, for which the radial force balance is fulfilled. Likewise, Equation 3.2.11 and 3.2.16 can be used to calculate the toroidal and poloidal current profiles I_{tor} and I_{pol} . As the poloidal current requires the magnetic field at the magnetic axis, where VMEC does not give reliable results, the partial poloidal current \tilde{I}_{pol} (Equation 3.2.16) can be computed instead.

The physically relevant input parameters to VMEC also specify an equilibrium, though not necessarily uniquely. The input in *fixed boundary mode* is the plasma boundary in terms of a Fourier series for R and Z at $\rho = 1$. Alternatively, in *free boundary mode* the background magnetic field described by a set of coils and their coil current ratios are required. Additionally, the pressure profile $p(\rho)$ needs to be specified, as well as

¹As described in Section 1.5.1, VMEC uses the left-handed (ρ, θ, ζ) coordinates which can be converted to right-handed (ρ, ϑ, ζ) coordinates.

either the rotational transform profile $\iota(\rho)$ or the toroidal current $I_{\text{tor}}(\rho)$. The scalar parameters ψ_0 and N_{FP} need to be supplied as well. Consequently the pressure and current profiles, together with coil current ratios, ψ_0 and N_{FP} also define an equilibrium, without describing it directly.

4.2 Dimensionality reduction

With $K = 99$ flux surfaces, $M = 11$ poloidal modes, $N = 12$ toroidal modes and taking into account that some Fourier coefficients are always 0, a VMEC equilibrium contains 85348 parameters, where the necessary number of modes and flux surfaces are determined by the complexity of the plasma configuration and desired resolution. This specific resolution was chosen in the equilibrium reconstruction framework for the standard configuration of the stellarator Wendelstein 7-X (W7-X) presented in Chapter 5. A probability distribution of VMEC equilibria of this resolution would therefore need 85348 dimensions, which is too many for practical purposes. The number of dimensions increases the required amount of storage space for samples representing a distribution linearly. The required computations and storage for a description of the probability density itself, typically scale exponentially with the number of dimensions. As such, it is important to keep the dimensionality as low as possible while still describing the distribution accurately.

While the data of interest consists of the five quantities ψ_0 , R_{kmn} , Z_{kmn} , λ_{lmn} and ι_k (as N_{FP} is usually constant), it can be arranged into a *feature vector* \mathbf{q} by flattening and stacking the components of the five base quantities. A distribution of equilibria is equivalent to a distribution of such a feature vector, which is described with a collection of samples drawn from the target distribution. This data matrix Q can then be projected to the *latent space* defined by the *principal components* using PCA as described in Section 1.6.

As the PCA determines the importance of the principal components based on the amount of variance they explain, care needs to be taken when assembling the feature vector \mathbf{q} from different quantities. The five quantities do not have the same units and also contain a different number of features, i.e. ψ_0 is a scalar, R_{kmn} is made up of almost² $K \cdot M \cdot (2N + 1)$ values and ι_k contains K values. The five quantities were therefore rescaled with their respective variances, such that they each contribute equally to the total variance and the different units also cancel out. Additionally, it is possible to multiply weight factors to each quantity, in order to assign a higher or lower importance to one of them.

4.3 Probability density estimation

In the typical usecase, the prior and posterior probability distributions over MHD equilibrium parameters are not stored in a functional form, but rather as samples drawn from these distributions. One way these samples can be obtained is described in Chapter

²For some modenumbers the corresponding values of R_{kmn} , Z_{kmn} and λ_{kmn} are 0 due to symmetry.

5. The functional form of these distributions is unknown, but can be approximated with a density estimation. If nonlinear correlations are neglected, PCA finds a subspace with independently distributed variables. Under this assumption, a *kernel density estimation* (KDE) can be applied to each latent dimension individually and the full distribution can be described by a tensor product over all KDEs. While this assumption seems to be mostly true for the case presented in Chapter 5, the small nonlinear correlations might introduce errors as the distribution can now cover unphysical regions of the parameter space. The extent of these errors likely depends on the distribution in question.

An alternative approach uses a *normalizing flow* [20] to approximate the latent probability density distribution. A normalizing flow is a trainable sequence of invertible and differential mappings between the target distribution and a base distribution, that is commonly chosen to be a Gaussian distribution. The parameters of this transformation are trained by minimizing the Kullback-Leibler divergence of the transformed samples to the Gaussian distribution. The assessment of the quality of density estimation via normalizing flows, in comparison to the tensor product KDEs is still ongoing for the dataset of W7-X equilibria considered in this work. However, the underlying problem is that any multi-dimensional approximation of the latent probability density distribution will require significantly more samples than the approximations for each dimension independently.

4.4 Quality assessment

In this section, the quality of the dimensionality reduction shall be assessed. This is done by computing the difference between a quantity \mathbf{Q} and its value $\tilde{\mathbf{Q}}$ after it has been projected to the latent dimensional space. The chosen metric for the *absolute error* ΔQ is the L^2 -norm

$$\Delta Q = \sqrt{\sum_i (Q_i - \tilde{Q}_i)^2}, \quad (4.4.1)$$

where i enumerates the features of the quantity \mathbf{Q} , i.e. the mode numbers and flux surfaces. While the absolute error has the same units as the quantity itself, it is the sum of all local squared errors³ and as such depends on the resolution of the quantity \mathbf{Q} . To be interpretable as a measure of quality, it needs to be related to the *magnitude* of \mathbf{Q} . The *relative error* δQ is then

$$\delta Q = \frac{\Delta Q}{|\mathbf{Q}|} = \frac{\sqrt{\sum_i (Q_i - \tilde{Q}_i)^2}}{\sqrt{\sum_i Q_i^2}}, \quad (4.4.2)$$

where the normalization makes δQ unitless and independent on the resolution of \mathbf{Q} .

For the following analysis, data from the *SurroBIER* equilibrium reconstruction workflow on W7-X [18], also described in Chapter 5, was used. The data encompasses 4000 3D

³The sum of the squared fourier coefficients R_{mn} , Z_{mn} and λ_{mn} corresponds to an L^2 integration, but it disregards the weighting of the volume element with the Jacobian \mathcal{J} . As such ΔQ does not correspond to a flux surface integral.

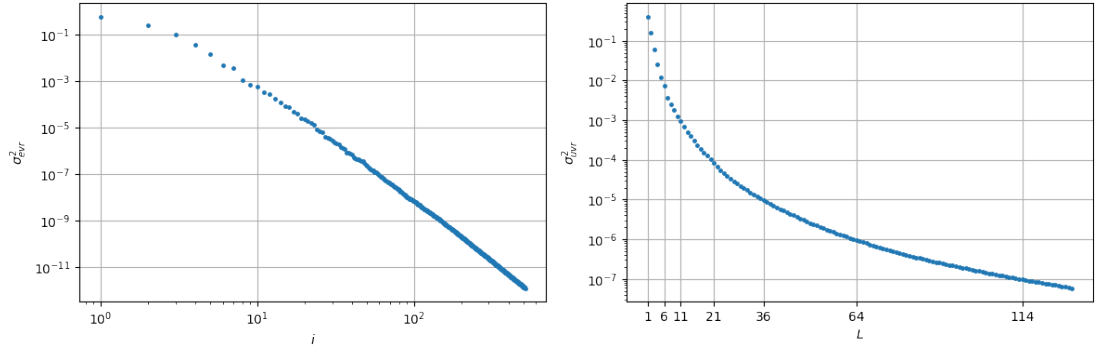


Figure 4.1: Explained variance ratio σ_{evr}^2 of the i -th principal component (left) and unexplained variance ratio σ_{uvr}^2 for the projection to L latent dimensions (right).

MHD equilibria for W7-X, calculated with VMEC from a rather wide prior distribution of pressure and current profiles. VMEC was run in *free boundary mode* with a background magnetic field specified by the coil currents i_1 to i_5 in the so called *standard configuration* for W7-X. The resolution of VMEC was chosen with 99 flux surfaces, poloidal mode numbers up to $M = 11$ and toroidal mode numbers between positive and negative $N = 12$. Neglecting coefficients which are constant, each equilibrium is then described by 85348 features. The main quantities of interest are the base quantities ψ_0 , R , Z , λ and ι , as well as the consistent pressure gradient and current profiles $\frac{dp}{d\rho}$, I_{tor} and \tilde{I}_{pol} . The profiles are calculated with the formulas presented in Chapter 3 and evaluated with the finite difference scheme using a half mesh, as detailed in Section 3.3.

4.4.1 Explained variance ratio

The main parameter of interest is the number of latent dimensions L . With $L = \min(S, F)$, PCA is a basis change and an exact representation of the original data⁴. The advantage of using PCA is however the ability to do *dimensionality reduction*, that is, representing the data with as few dimensions as possible, while preserving as much of the relevant information as possible. The principal components are usually ordered with decreasing explained variance ratio $\sigma_{evr,l}^2 = \Lambda_l$, shown in Figure 4.1 to the left. Commonly, the unexplained variance ratio (Equation 1.6.8) is used to determine the number of retained latent dimensions L , as shown in Figure 4.1 to the right. As additional principal components give diminishing amounts of explained variance, but the amount of data needed to describe a collection of samples rises linearly, choosing as few latent dimensions as feasible becomes very important. The computational costs and required amount of samples to cover a volume of phase space, often even increase exponentially, making dimensionality reduction even more important.

⁴In practice it is limited to machine precision.

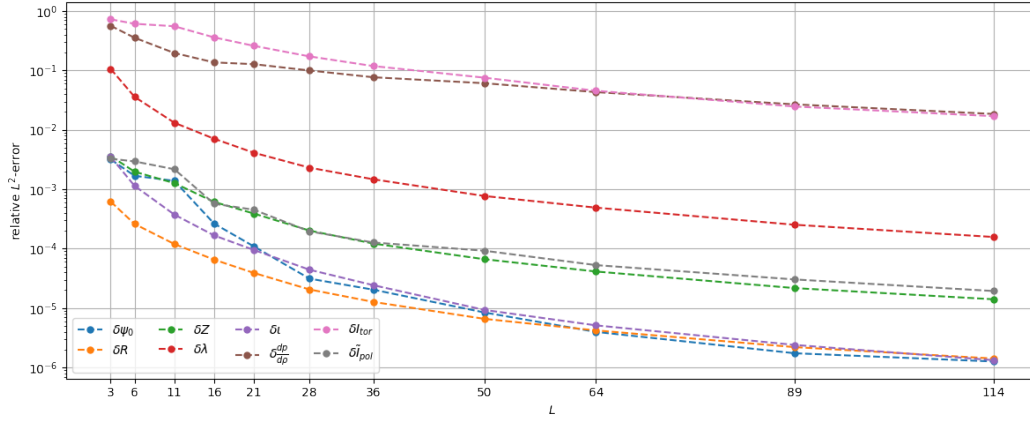


Figure 4.2: Median relative L^2 -error for the total toroidal flux ψ_0 , the inverse coordinate maps R, Z and λ , the rotational transform ι , pressure gradient $\frac{dp}{d\rho}$, toroidal current I_{tor} and partial poloidal current \tilde{I}_{pol} profiles as functions of the number of latent dimensions L .

From Figure 4.1 it can be seen that 6 principal components represent 99% of the variance and 11 represent 99.9%, but the curve quickly flattens with 99.99% already requiring 21 principal components. While 114 latent dimensions, corresponding to an unexplained variance ratio of 10^{-7} , are a tremendous improvement over the $\sim 8 \cdot 10^4$ original dimensions, many statistical methods work best with a number of dimensions below 10. As such, applications like the equilibrium reconstruction using surrogate models [18] presented in Chapter 5, are limited to the 99.99% explained variance provided by 11 latent dimensions.

4.4.2 Reconstruction error of the base quantities

The explained variance ratio describes how much variance is preserved with dimensionality reduction, not necessarily how well the data and relevant physics are preserved⁵. The relative error in Equation 4.4.2, is a measure for the degree at which information is preserved in dimensionality reduction, relative to the magnitude of the quantity in question itself. The relative error can now be compared between the different base quantities and consistent profiles. The median relative L^2 -error for the whole dataset, reduced to the different numbers of latent dimensions, is shown in Figure 4.2.

The relative error decays for all quantities with increasing L , as expected. In Figure 4.3 the distribution of the error is shown for 11 latent dimensions. From this, it can be seen that each distribution is monomodal around the median and the relative error spans up to two orders of magnitude. It can also clearly be seen that, while the base quantities are preserved with an accuracy of 10^{-4} to 10^{-2} , the consistent profiles are mostly not

⁵However, it can be shown that PCA is equivalent to minimizing the least squares error for a linear subspace.

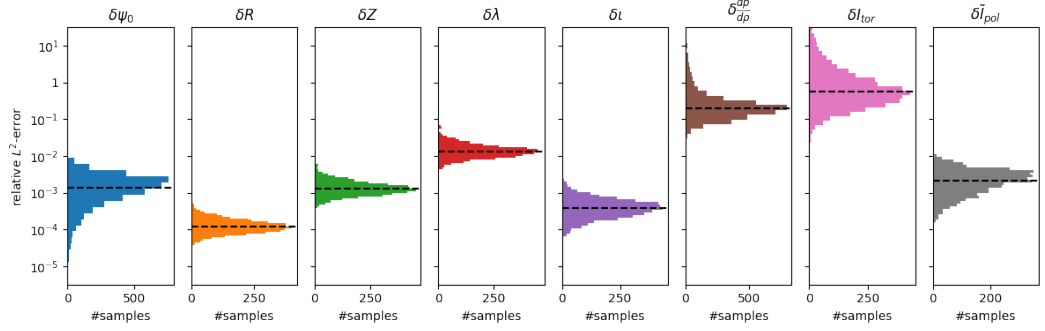


Figure 4.3: Histogram of the relative L^2 -error (Equation 4.4.2) for the total toroidal flux ψ_0 , the inverse coordinate maps R, Z and λ , the rotational transform ι , pressure gradient $\frac{dp}{d\rho}$, toroidal current I_{tor} and partial poloidal current \tilde{I}_{pol} profiles for 11 latent dimensions, corresponding to 99.99% of the explained variance. The black dashed line shows the median of each distribution.

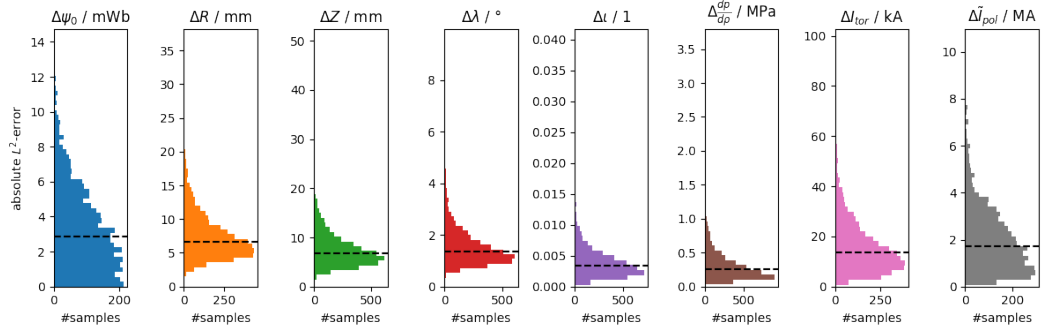


Figure 4.4: Histogram of the absolute L^2 -error (Equation 4.4.1) for the total toroidal flux ψ_0 , the inverse coordinate maps R, Z and λ , the rotational transform ι , pressure gradient $\frac{dp}{d\rho}$, toroidal current I_{tor} and partial poloidal current \tilde{I}_{pol} profiles 11 latent dimensions, corresponding to 99.99% of the explained variance. The black dashed line shows the median of each distribution.

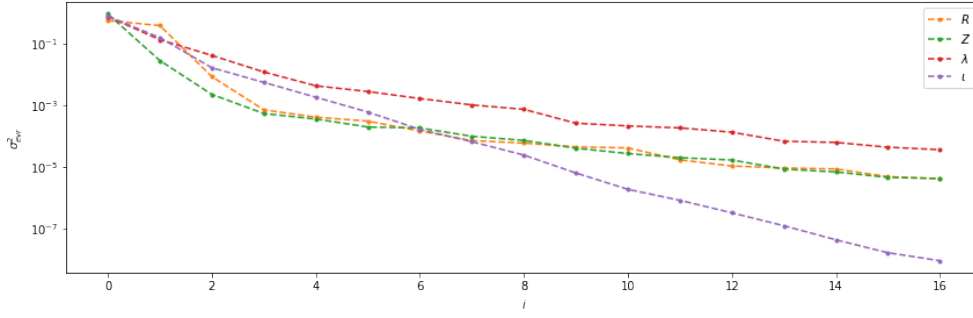


Figure 4.5: Comparison of the explained variance ratio σ_{err}^2 of the principal component i for the PCA of the inverse coordinate maps R , Z and λ as well as the rotational transform ι individually.

preserved at all. From the absolute error in Figure 4.4, it can be seen that the error in R and Z is very similar, but the magnitude of R is much larger as it is approximately the major radius of the torus, while Z is the minor radius at maximum. The absolute error also provides a more accessible error metric as the total error in the flux surface positions is in the order of centimeters.

The five base quantities were rescaled before applying the PCA such that their contribution to the total variance was the same (Section 4.2) and yet the degree to which they are preserved is not. Especially λ shows a large relative error. A possible reason for this is that λ is distributed more broadly, i.e. that the variance of the distribution of λ is spread over a higher number of principal components when PCA is applied to each quantity individually, as seen in Figure 4.5. The correlation between the individual unexplained variance ratios and the relative error can indeed be seen as both decrease the fastest for ι (with the exception of the error for the scalar parameter ψ_0) and decrease the slowest for λ .

4.4.3 Reconstruction error of the consistent profiles

The consistent pressure gradient $\frac{dp}{d\rho}$ and toroidal current I_{tor} in Figure 4.2 show much larger errors than the base quantities, while the partial poloidal current \tilde{I}_{pol} is preserved with similar accuracy to ψ_0 and Z . However, these errors decrease as the number of latent dimensions L increases. In particular, with 36 latent dimensions, corresponding to an explained variance ratio of 99.999%, the median relative error has decreased below 10%. With 114 latent dimensions, corresponding to an explained variance ratio of 99.99999%, the median relative error of $\frac{dp}{d\rho}$ and I_{tor} still amounts to a few percent. Figure 4.3 also shows that while the relative error distribution of R , Z , λ and ι is roughly a single order of magnitude wide, it is much wider for $\frac{dp}{d\rho}$ and I_{tor} . In particular, this means that even if the median error for $L = 36$ amounts to 10%, there will be a significant number of samples, for which the error will be larger than the magnitude of $\frac{dp}{d\rho}$ or I_{tor} itself.

While the consistent profiles depend on the base quantities in a non linear manner (Chapter 3), it is not immediately obvious why the errors are that large and in particular, why the partial poloidal current is not affected that much. A closer inspection of the intermediate quantities in the calculation of the profiles, in particular the poloidal and toroidal magnetic fields B_θ and B_ζ , is shown in Figure 4.6. The first observation is that the relative error of the local magnetic field components B_θ and B_ζ is actually preserved well, with a similar accuracy as ψ_0 or Z at the same dimensionality $L = 11$ (Figure 4.3). The second observation is that the absolute errors for each of the components stays roughly the same through integration and differentiation.

For the poloidal component B_θ , the sudden increase in the relative error happens during integration. This can be explained by considering, that a stellarator like W7-X is actually optimized to have a low toroidal current $I_{\text{tor}} \propto \langle B_\theta \rangle$, but that does not mean the local current density and therefore poloidal magnetic field is small. On the contrary, both may not be too small compared to the toroidal field, to ensure good confinement.

For the toroidal component B_ζ , the integration does not change the magnitude or the relative error, but the radial derivative does. As the pressure gradient depends on the derivatives of both currents, this is a main contribution to its high error. The main reason the derivative changes the magnitude so much, is that the toroidal magnetic field does not vanish at the magnetic axis, but is rather only weakly dependent on the radial position. Therefore the radial derivative is much smaller than the magnitude of the toroidal magnetic field itself. Finally, the absolute error of the toroidal magnetic field and therefore poloidal current gradient, is much larger than that of the toroidal current gradient. As both profiles contribute almost equally to the pressure gradient, the relative error in the pressure gradient profile is dominated by the error of the poloidal current gradient, as can be seen in their similar shape.

4.4.4 Resolution of flux surface integrals

A free parameter in the calculation of the consistent profiles is the resolution of poloidal and toroidal grid points for the integration over the flux surfaces. The number of toroidal grid points can be significantly reduced by restricting the computational domain to a single toroidal field period and multiplying the resulting integral with the number of field periods N_{FP} . For each of the equilibria in the dataset, the profiles were calculated with varying resolutions until convergence was observed. Figure 4.7 shows the median relative error of the three consistent profiles as functions of the poloidal and toroidal resolution, where both directions were resolved with the same number of points. In this case, the error is the difference between the consistent profiles and the input profiles that were supplied to the equilibrium solver VMEC⁶. It can be seen that starting from about 18 integration points in each direction, the error converges. With 25 integration points the integration can be assumed to be sufficiently converged.

⁶Note that the profile values at the boundaries cannot be calculated with the current implementation of the finite difference scheme and were therefore omitted from this analysis. Also note that VMEC shows systematic errors in the profiles, especially near the magnetic axis. These systematic errors determine to a large extend the minimum error to which the total error converges.

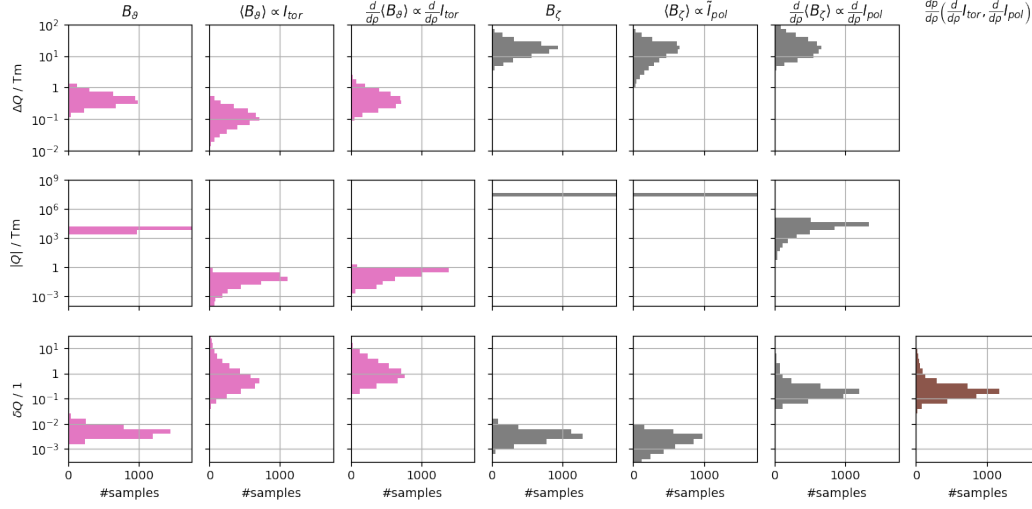


Figure 4.6: Histogram of the absolute and relative L^2 -error (Equation 4.4.1 and 4.4.2) as well as the magnitude $|Q|$ for the covariant poloidal and toroidal magnetic field components B_θ and B_ζ , their integrals over flux surfaces and subsequent radial derivatives for 11 latent dimensions. Additionally, the relative L^2 -error of the pressure gradient profile (Equation 3.1.32) is shown.

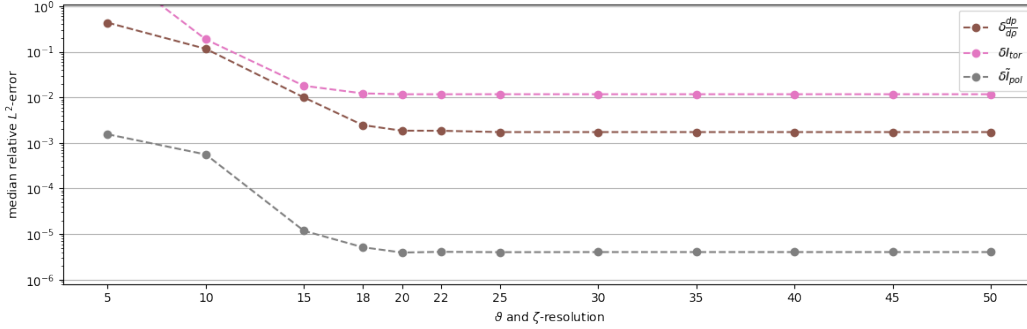


Figure 4.7: Median relative L^2 -error for the consistent pressure gradient $\frac{dp}{d\rho}$, toroidal current I_{tor} and partial poloidal current \tilde{I}_{pol} profiles for varying poloidal and toroidal resolution.

4.4.5 Visual interpretation

While Figure 4.4 gives some insight for the interpretation of the errors, e.g. that the locations of the flux surfaces, determined by R and Z , are preserved with an accuracy in the mm range for $L = 11$, even more insight can be obtained from the visual interpretation of a single sample equilibrium, as shown in Figure 4.8. Here the main quantities of interest are shown for projections to different numbers of latent dimensions. In particular 11, 34 and 100 dimensions are plotted, corresponding to an unexplained variance ratio of about 10^{-3} , 10^{-5} and 10^{-7} respectively.

For the overall flux surface geometry, (top left) 11 latent dimensions are enough such that no difference to the original equilibrium is visible. In a zoomed poloidal cut at a position of high curvature, (top center) the flux surfaces at $L = 11$ deviate from the original ones by a few cm maximum. With 34 latent dimensions, no difference can be observed. For the rotational transform profile ι , (top right) 11 latent dimensions are again enough. The consistent pressure gradient and toroidal current profiles, (bottom left and center) are preserved poorly according to Figures 4.2 and 4.3. Visually this can be confirmed as the profiles corresponding to $L = 11$ follow the original trend only in a broad approximation. With $L = 34$, the overall shape is mostly preserved, but significant errors are still present. Finally, with 100 latent dimensions, the profiles are preserved with adequate accuracy apart from a deviation at the plasma boundary for the pressure gradient. The poloidal current profile shows the correct shape at 11 dimensions, but is offset from the correct background magnetic field. With 34 latent dimensions this is no longer the case and the profile is preserved up to small deviations.

Figure 4.8 highlights that the usecase and thereby the requirements concerning the different quantities and computational costs, are the main points of consideration when choosing the number of latent dimensions. If the flux surface geometry should be determined approximately or the computational costs and space requirement are limiting, less than 11 latent dimensions can be enough. For an accurate geometry and approximate consistent profiles the applied methods need to be able to work with about 34 dimensions. An accurate representation of the consistent profiles with 100 latent dimensions places hard restrictions on the methods which are capable of handling this dimensionality. Finally, it should be noted that this analysis uses data from the standard configuration of W7-X and the situation might be different for other configurations.

4.5 Improvements using the pressure gradient

One idea for improving the quality of the dimensionality reduction is reweighing the PCA by adding redundant data to the base quantities. In particular, the quality of the consistent pressure gradient $\frac{dp}{d\rho}$ is found to be much worse than the base quantities ψ_0 , R , Z , λ and ι . Including $\frac{dp}{d\rho}$ in the PCA gives two opportunities:

On one hand, it is now possible to expand the latent variables to an equilibrium including the pressure gradient and it is not necessary to calculate it with Equation 3.1.32. While this saves computational time, the radial force balance (Equation 3.1.31)

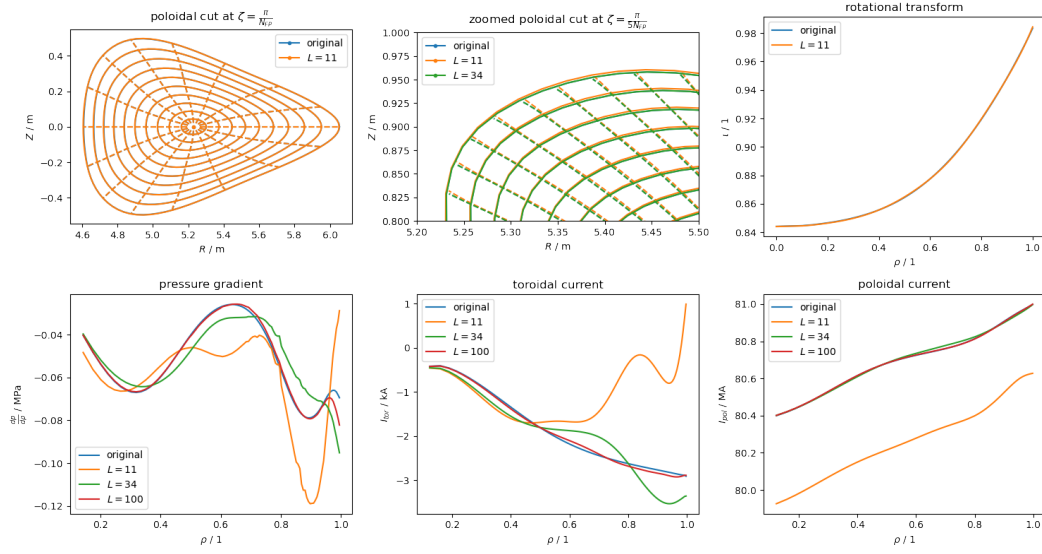


Figure 4.8: Visual comparison of the flux surface geometry (top left and top middle), containing the inverse coordinate maps R, Z and λ , the rotational transform ι (top right), pressure gradient $\frac{dp}{d\rho}$ (bottom left), toroidal current I_{tor} (bottom middle) and poloidal current \tilde{I}_{pol} (bottom right) profiles for a single equilibrium reduced to different number of latent dimensions L .

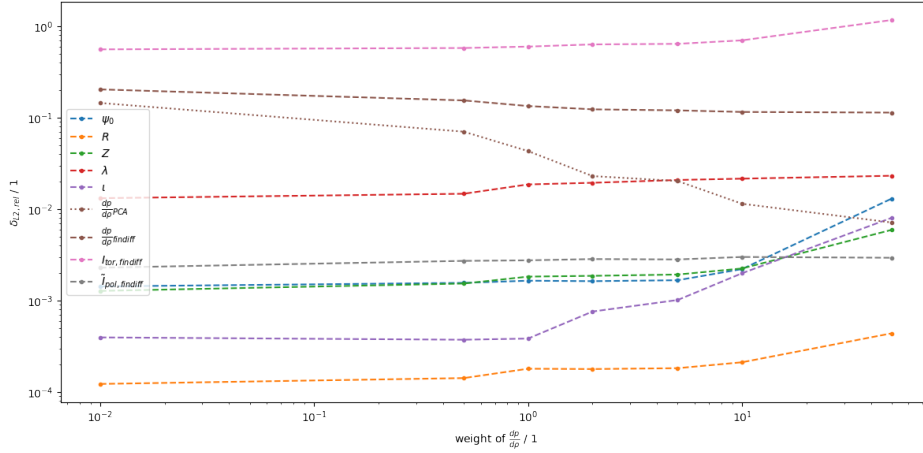


Figure 4.9: Median relative L^2 -error for the total toroidal flux ψ_0 , the inverse coordinate maps R, Z and λ , the rotational transform ι , expanded and consistent pressure gradient $\frac{dp}{d\rho}_{\text{PCA}}$ and $\frac{dp}{d\rho}_{\text{findiff}}$, toroidal current I_{tor} and partial poloidal current \tilde{I}_{pol} profiles as functions of the weight of $\frac{dp}{d\rho}$ in the PCA with $L = 11$ latent dimensions.

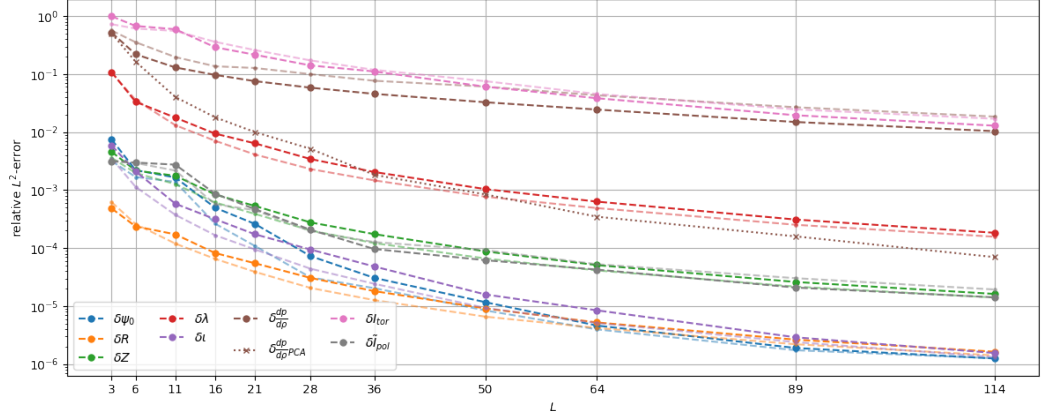


Figure 4.10: Median relative L^2 -error for the total toroidal flux ψ_0 , the inverse coordinate maps R, Z and λ , the rotational transform ι , consistent and included pressure gradient $\frac{dp}{d\rho}$ and $\frac{dp}{d\rho_{\text{PCA}}}$, toroidal current I_{tor} and partial poloidal current \tilde{I}_{pol} profiles as functions of the number of principal components L for a PCA including $\frac{dp}{d\rho}$ with equal weight. The transparent lines show the error without including $\frac{dp}{d\rho}$ in the PCA.

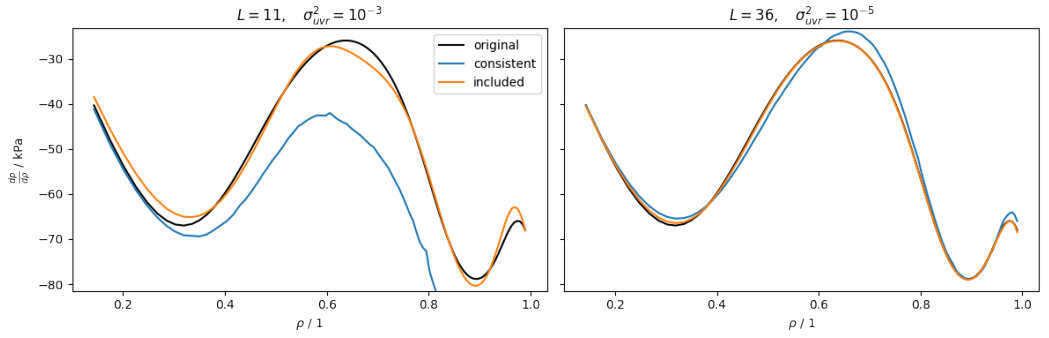


Figure 4.11: Comparison of the included and consistent pressure gradient $\frac{dp}{d\rho_{\text{PCA}}}$ and $\frac{dp}{d\rho_{\text{con}}}$ with the original pressure gradient of a single sample for 11 and 34 latent dimensions corresponding to an unexplained variance ratio of 10^{-3} and 10^{-5} respectively. The original $\frac{dp}{d\rho}$ profile was included in the PCA with equal weight.

can now be violated. For some applications, the resulting force balance error might still be acceptable, but other applications require consistent profiles⁷.

On the other hand, the inclusion of the pressure gradient in the PCA will reweigh the base quantities, such that the modes which contribute most to the radial force balance are represented more strongly in the first few principal components. Therefore, also the quality of the consistent pressure gradient is expected to improve. Finally, it is possible to assign a higher weight to the pressure gradient compared to the base quantities, to increase the strength of this effect.

Figure 4.9 shows exactly the behavior as expected, with the error of the base quantities and the other consistent profiles increasing as more weight is put on $\frac{dp}{d\rho}$, while the error of both the expanded and the consistent pressure profiles decrease. However the consistent pressure gradient improves only a little at 11 latent dimensions, and increasing the weight of $\frac{dp}{d\rho}$ in the PCA leads to no sizable improvement, while the error of the base quantities increases drastically. Figure 4.10 shows the dependence of the median relative error on the number of latent dimensions. Again the errors for ψ_0 , R , Z , λ and ι increase, while the errors of the consistent profiles decrease by a small amount. Contrary to preliminary investigations, where the pressure profile was included in the PCA, the quality of the included pressure gradient $\frac{dp}{d\rho}_{\text{PCA}}$ is better than the consistent profile. This essentially means that the included profile is closer to the original $\frac{dp}{d\rho}$ profile than the profile for which the radial force balance would be fulfilled exactly. This is shown in Figure 4.11, which visually compares the two profiles for a single equilibrium for 11 and 34 latent dimensions. In addition to the improved quality, the included profile does not require any additional computations during the projection from latent space to full equilibria. However for the application as a pressure diagnostic, the pressure at real space positions is required, which during preliminary investigations added significant computation time for inverting the coordinate mapping, such that computing the consistent pressure gradient is no longer the bottleneck.

4.6 Python implementation

A prototype of this framework for describing equilibrium distributions was implemented as the *EqDist*⁸ python package. It is designed to be used with the *SurroBIER* equilibrium reconstruction framework presented in Chapter 5.

Central to the package is the `EquilibriumDistribution` class which describes a collection of samples with their respective latent coefficients \mathbf{c} , together with the mean vector $\boldsymbol{\mu}$, principal components \mathbf{p} , rescaling factors σ^2 and weights w . This information is all that is required to expand the low dimensional representation back to the full parameters detailed in Section 4.1. Most data in the *EqDist* package is contained in `xarray` [16] `Datasets`, which allow convenient access to all parameters with named

⁷Note however that even if the radial force balance is fulfilled exactly, the local force balance does not have to be fulfilled.

⁸*EqDist* has not been published at the time of this writing. Please get into contact with the author or advisor to request access.

```

1 import numpy as np
2 import xarray as xr
3 import eqdist
4
5 # "VMECeqs.nc" is created from many VMEC output files with the 'collect.py' script
6 eqs = xr.open_dataset("VMECeqs.nc")
7 # create low dimensional representation with 99% explained variance retained
8 eqds = eqdist.EquilibriumDistribution.from_expanded(eqs, accuracy=0.99)
9
10 # expand equilibria to the high dimensional representation (same format as 'eqs')
11 expanded = eqds.expand()
12
13 # calculate the consistent pressure gradient and current profiles
14 expanded2 = eqdist.calc_profiles(expanded)
15
16 # compute divergence between reexpanded and original equilibria
17 recerr = eqdist.equilibrium_divergence(eqs, expanded, norm="L2")
18
19 # plot the flux surface geometry of sample no. 10 at zeta=pi/5
20 eqdist.plot_surf(eqs.sel(samples=10), zeta=np.pi/5)

```

Listing 4.1: Example code using the *EqDist* package.

indices and mirror the structure of the *netCDF* file format. The `collect` module and script provide utilities for reading the equilibria generated by VMEC, which can then be reduced to their low dimensional representation. The underlying functions `stack` and `unstack`, which handle the grouping of parameters and reshuffling of indices, such that the principal components can be described as simple vectors, have been designed to be flexible with respect to which particular parameters are used. This for example allows the inclusion of the pressure gradient in the PCA in a simple manner, but the implementation is not very robust due to technical limitations of the underlying library functions.

The *EqDist* package also contains several functions which act on a collection of high dimensional equilibria and can plot the flux surfaces, calculate the consistent pressure gradient and poloidal and toroidal currents or calculate the divergence with respect to another collection of equilibria. Robert Köberl has also expanded the package to invert the coordinate mapping, that is to provide methods which find the flux coordinates for given real space coordinates. Some example methods using the *EqDist* package are shown in Listing 4.1.

5 Magnetohydrodynamic equilibrium reconstruction

For experiments in a fusion reactor it is interesting to know the state of the plasma in terms of the MHD equilibrium during the experiment. The process of inferring a MHD equilibrium from diagnostic signals is called *equilibrium reconstruction*. In addition to the flux surface geometry and the current and pressure profiles, which make up the MHD equilibrium, the equilibrium is a frequent starting point for more detailed plasma models. The flux surface geometry often defines the coordinate system in which all other quantities are then described.

The key difficulty of equilibrium reconstruction is, that MHD solvers require the current and pressure profiles as inputs, but they need to be defined in terms of the normalized toroidal flux $s = \rho^2 \propto \psi$. The diagnostics can however only provide these profiles in real space, as the mapping between the real coordinates and the flux surface geometry is part of the MHD solution. Such a situation where the solution is part of the input is called a *fixed point problem*. For tokamaks like ASDEX Upgrade, equilibrium reconstruction is performed routinely [11, 12], but due to the inherent toroidal symmetry the MHD equations simplify (Section 2.1). For the 3D geometry of stellarators like Wendelstein 7-X (W7-X), equilibrium reconstruction traditionally is solved iteratively in a least squares sense [2, 22, 28]. A main difficulty of the 3D problem is the high computational costs of the forward model, which results in a single equilibrium reconstruction taking up to several hours. The least-squares approach gives suitable reconstructed parameters with uncertainty estimates [5], but high levels of noise in the equilibrium diagnostics can cause common error estimates to be unable to capture relevant uncertainties [19]. While existing Bayesian frameworks [35] also have the problem of the high computational cost of the forward model, there have been recent developments on a surrogate enhanced equilibrium reconstruction, which allows fast sampling from the posterior distribution. This new framework by Köberl, Babin, and Albert [18] uses the low dimensional representation of MHD equilibria presented in Chapter 4 and is described in this chapter.

5.1 Reconstruction framework

In contrast to solving the fixed point problem with an iterative procedure, this framework aims to apply Bayesian Inference (Section 1.7), by reformulating equilibrium reconstruction as an inverse problem. To reiterate, Bayes' rule

$$p(Q | d, \mathcal{I}) \propto \mathcal{L}(d | Q) \pi(Q) \quad (5.1.1)$$

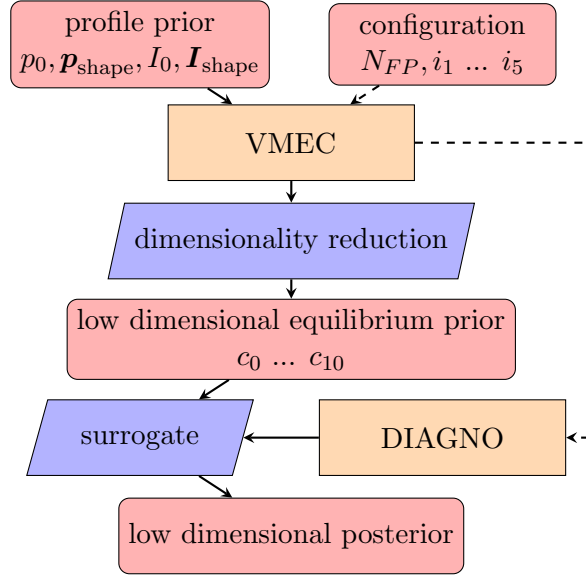


Figure 5.1: Overview of the proposed framework. Reproduced from Köberl, Babin, and Albert [18].

allows the calculation of the posterior distribution $p(\mathbf{Q} | \mathbf{d}, \mathcal{I})$ for the equilibrium parameters \mathbf{Q} , depending on the measured diagnostic signals \mathbf{d} , from the prior distribution $\pi(\mathbf{Q}) := p(\mathbf{Q} | \mathcal{I})$ and the likelihood function $\mathcal{L}(\mathbf{d} | \mathbf{Q}, \mathcal{I}) := p(\mathbf{d} | \mathbf{Q}, \mathcal{I})$. For generating samples from the posterior distribution, the normalizing factor $p(\mathbf{d} | \mathcal{I})$, called *evidence*, can often be omitted. This still leaves two challenges to be addressed: First, a prior distribution of equilibrium parameters needs to be found. In particular, this is problematic as there is no simple physical intuition for the many parameters needed to describe an equilibrium. However, it is important to restrict the prior to sensible and realistic equilibria and additionally keep the number of dimensions as low as possible, to minimize the computational costs. The second challenge is the formulation of a fast likelihood function. In order to draw samples from the posterior distribution, in contrast to just finding the best fit, many thousands of likelihood evaluations need to be done. It is therefore important to make the likelihood evaluation as fast as possible while keeping adequate precision.

The proposed framework [18] and previous work [19] suggest the following solution to these challenges, displayed graphically in Figure 5.1: While the prior distribution on equilibrium parameters is hard to formulate intuitively, the related prior distribution of current and pressure profiles can be formulated. Sampling this distribution of profiles and solving for the MHD equilibrium for each sample, results in a distribution of equilibria which are then reduced to a more manageable number of dimensions. A density estimation in the low dimensional space then yields a formulation for the prior distribution of equilibrium parameters $\pi(\mathbf{Q})$. For the collection of MHD equilibria the synthetic diagnostics are evaluated, which make up the computationally most demanding

part of the likelihood evaluation. Subsequently, surrogate models are trained for the diagnostics, dependent on the low dimensional coefficients. With these models, the likelihood evaluation during the inference is sped up significantly.

5.2 Equilibrium prior distribution

To solve the MHD Equations 1.2.8-1.2.10 under *free boundary conditions*, several ingredients are required: While the number of field periods N_{FP} is constant for each device and the background magnetic field, e.g. specified by the coil currents i_1 to i_5 for W7-X, is usually constant for an experiment or even a series of experiments, the pressure profile $p(s)$, toroidal current profile $I_{\text{tor}}(s)$ and total toroidal flux ψ_0 can take a wide range of values and shapes. Note that the profiles are specified in terms of the radial flux coordinate $s = \rho^2 \propto \psi$, which is a major reason why equilibrium reconstruction is that difficult. However the range of expected values and the expected shapes of the profiles are known from experience and should now be encoded in a prior distribution.

A simple description of a distribution of functions can be achieved by using a *Gaussian Process* (GP), as introduced in Section 1.7.1, following similar concepts realized in the MINERVA framework for W7-X [24, 26, 35]. In contrast to other equilibrium reconstruction methods [5, 19, 22, 28], which often use simple parameterized functions to describe the profiles, a GP allows for very flexible functions while prescribing certain properties. The main properties of interest are the boundary conditions, differentiability and typical length scales, as well as non-negativity or monotonicity. The pressure profile has its maximum at the magnetic axis and decays to zero at the plasma boundary. The correlation length scales are typically larger in the core of the plasma than at the boundary, which is encoded in the GP kernel introduced in the MINERVA framework [24]. Furthermore, the pressure profile is constrained to be monotonically decreasing. These constraints are achieved by modeling the shape function with an unrestricted Gaussian Process and subsequent exponentiation, integration and renormalization. The exponentiation ensures the monotonicity, while allowing for steep gradients and discouraging many local plateaus:

$$p_{\text{shape}}(s) \sim \mathcal{GP}_{\text{Minerva}} \quad (5.2.1)$$

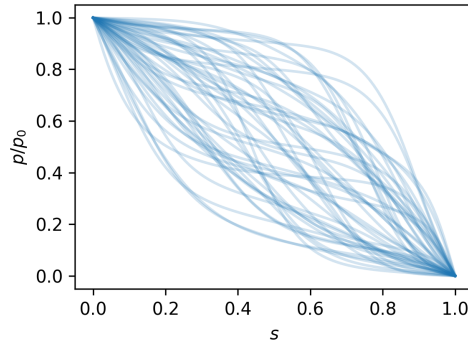
$$\tilde{p}(s) = \int_s^1 \exp(p_{\text{shape}}(s')) ds' \quad (5.2.2)$$

$$p(s) = \frac{p_0}{\tilde{p}(0)} \tilde{p}(s). \quad (5.2.3)$$

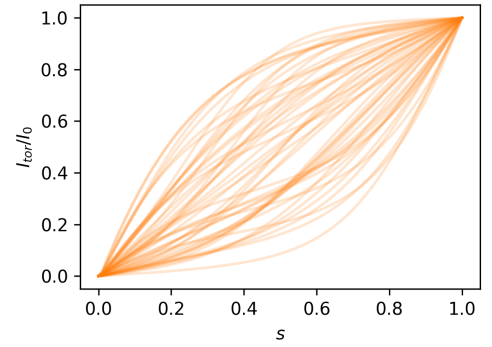
The toroidal current profile has similar restrictions, but vanishes at the magnetic axis while reaching the maximum at the boundary. It is rather hard to measure experimentally, which is why a simpler, *rational quadratic GP* [27] is used instead. This kernel uses an uniform correlation length, but still allows a range of length scales. Again exponentiation and integration ensure monotonicity and renormalization decouples the shape distribution

Table 5.1: The chosen prior parameters and their distribution. Reproduced from Köberl, Babin, and Albert [18].

| Symbol | Distribution | Description |
|-----------------------------|----------------------------------------------------------------------------------------------------------------------------------------------------------------------------------|---------------------------------------------------------------------|
| ψ_0 | Uniform in $[-2.5 \text{ Wb}, -1.6 \text{ Wb}]$ | total toroidal magnetic flux |
| p_0 | Uniform in $[0, 200 \text{ kPa}]$ | pressure at the magnetic axis |
| $\mathbf{p}_{\text{shape}}$ | $\mathcal{GP}_{\text{Minerva}} \left(\begin{array}{l} \sigma_f = 1 \\ \lambda_{\text{core}} = 0.2 \\ \lambda_{\text{edge}} = 0.1 \\ s_0 = 0.9 \\ s_w = 0.1 \end{array} \right)$ | pressure profile shape factors reduced to 6 principal components |
| I_0 | Uniform in $[-10 \text{ kA}, 10 \text{ kA}]$ | total toroidal current |
| $\mathbf{I}_{\text{shape}}$ | $\mathcal{GP}_{\text{RQ}} \left(\begin{array}{l} \sigma = 2 \\ \lambda = 0.2 \\ \alpha = 2 \end{array} \right)$ | current profile shape factors reduced to 3 principal components |



(a) Normalized pressure profiles.



(b) Normalized toroidal current profiles.

Figure 5.2: Samples drawn from the prior distribution of the normalized pressure and toroidal current profiles. Reproduced from Köberl, Babin, and Albert [18].

from the magnitude:

$$I_{\text{shape}}(s) \sim \mathcal{GP}_{\text{RQ}} \quad (5.2.4)$$

$$\tilde{I}(s) = \int_0^s \exp(I_{\text{shape}}(s')) ds' \quad (5.2.5)$$

$$I_{\text{tor}}(s) = \frac{I_0}{\tilde{I}(0)} \tilde{I}(s). \quad (5.2.6)$$

The specific parameters chosen for W7-X are given in Table 5.1 and a number of samples from the pressure and current profile shapes, i.e. normalized without p_0 and I_0 , are shown in Figure 5.2.

For the purpose of effective sampling, the infinite dimensional GPs are approximated with a 6 and 3-dimensional PCA (Section 1.6) respectively. This then allows drawing

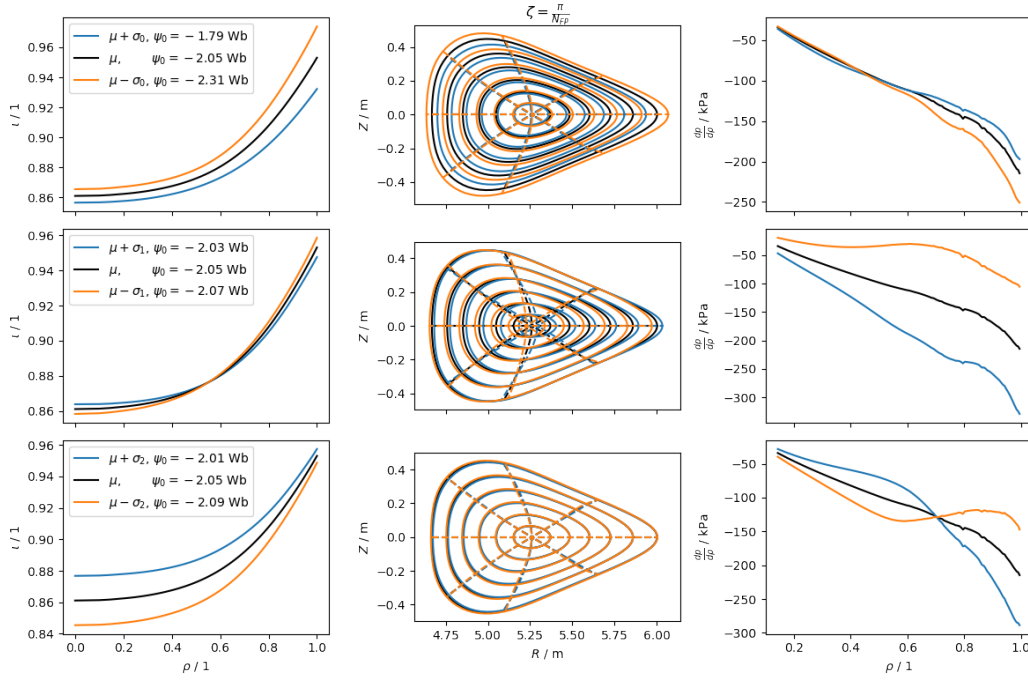


Figure 5.3: Rotational transform profile $\iota(\rho)$, flux surface geometry at the toroidal angle $\zeta = \pi$ and consistent pressure gradient profile $\frac{dp}{d\rho}(\rho)$ for the mean vector (black) and the positive and negative standard deviation in latent space for the first three principal components c_0 to c_2 . The value of the total toroidal flux ψ_0 is given in the legend.

4000 samples with the space-filling *latin hypercube* method, which serve as input for the 3D MHD solver VMEC [15] (Section 1.5). The result is a collection of sample equilibria, each specified by a large number of parameters, as detailed in Section 4.1. With PCA, as detailed in Section 4.2, the equilibria can then be projected to 11 latent dimensions, preserving 99.9% of the variance. As seen in Section 4.4, 11 principal components are enough to represent the flux surface geometry accurately, but introduce large errors in the consistent pressure gradient and current profiles.

5.2.1 Visual Interpretation

The principal components span a linear vector space, called the latent space, which contains most of the variation present in the data, but lack direct physical interpretability. The principal components themselves cannot be meaningfully projected back into the space of high dimensional equilibrium parameters, but they can be visualized by projecting $\mu \pm \sigma_i \mathbf{p}_i$, where μ is the mean equilibrium, \mathbf{p}_i the i -th principal component and σ_i the standard deviation of the i -th latent variable.

Figure 5.3 shows a visual representation of the equilibrium defining parameters and consistent pressure gradient profile for the mean equilibrium, as well as the positive and negative standard deviation for the first three principal components. In Figure 5.3, c_0 is strongly correlated with ψ_0 and therefore also strongly scales with the plasma volume and the spacing of the flux surfaces, while the pressure gradient and shape of the flux surfaces stays mostly the same and ι is shifted almost by a constant. c_1 seems to be strongly correlated with the pressure scaling present in the prior distribution. This can be seen as c_1 scales with the pressure gradient in the outer flux surfaces, which in turn change the pressure maximum and this is connected to the movement of the magnetic axis described by the Shafranov shift [31]. The plasma volume, ψ_0 and ι profile stay mostly the same.

The higher components starting with c_2 represent a much lower variance and their effects are harder to interpret. c_2 scales with the ι profile in the plasma core and changes the shape of the pressure gradient, between a steeper or more flattened plateau, while keeping the total pressure, plasma volume and ψ_0 mostly constant. The flux surface shape also changes, but only very little, consistent with the observed changes in the pressure gradient. Additionally, the prior distribution of c_0 and c_1 (also shown in Figure 5.6) follow a rather flat distribution, just like the uniform distribution of ψ_0 and p_0 in Table 5.1. In contrast, the higher components show a peaked distribution, just like the profile shape parameters, which all follow a Gaussian distribution.

5.3 Surrogate models for synthetic diagnostics

For W7-X there are many different diagnostics available. For this model three different sets of magnetic coils were used: *diamagnetic flux loops*, *saddle coils* and *segmented Rogowski coils* [8]. The position of these coils is shown in Figure 5.4 together with the flux surfaces of a typical equilibrium. For each sampled MHD equilibrium, the synthetic diagnostic code DIAGNO [21] is used to determine the expected diagnostic signals for each coil.

To enable a fast evaluation of the synthetic diagnostics in the whole parameter space, the calculations are fitted using *polynomial chaos expansion* (PCE). PCE uses a linear regression with a polynomial basis, where the basis polynomials are chosen based on the distribution of training data. The latent variables are assumed to be independent so that the prior probability distribution of the latent variables can be approximated by a tensor product of the *kernel density estimates* (KDE) of each dimension. The principal components are constructed to be linearly independent, but the non-linear dependence introduces additional errors in this approximation. Note however that this will primarily cause the distribution to be wider, which is only a problem if the approximated latent space now covers a region where the physically motivated constraints are violated, e.g. by having a positive pressure gradient. The full set of basis polynomials for the PCE was further restricted using a *hyperbolic truncation* scheme [3]. The quality of the resulting surrogate models is shown in Figure 5.5. All surrogates have a relative leave-one-out

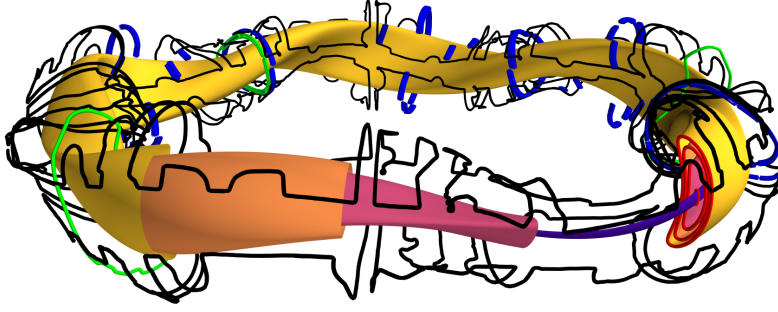


Figure 5.4: The flux surfaces of a standard MHD equilibrium configuration of W7-X together with saddle coils (black), diamagnetic flux loops (green) and segmented Rogowski coils (blue). Image courtesy of Robert Köberl.

error below 2% of the prior variance and a few diamagnetic flux loops show a much lower error. They probably measure the total toroidal flux ψ_0 almost directly.

5.4 Inference

With the prior distribution of the low dimensional latent variables and the fast likelihood using the surrogate models, all requirements for Bayesian inference are available. All the presented components were implemented in python using the *PyMC* [1] and *chaospy* [10] packages and grouped together in the *SurroBIER*¹ package.

Another sample was drawn from the prior distribution and propagated through VMEC and DIAGNO. This sample was taken as a known ground truth and the diagnostic output from DIAGNO was taken as if they were measured diagnostic signals. Figure 5.6 shows the results of the inference on the latent variables. The ground truth lies for every coefficient in a region of high probability and the posterior distribution is significantly narrower than the prior, at least for the latent variables c_0 to c_3 . This suggests that the method indeed works. However, while the Laplace's approximation shows a similar maximum than the full posterior distribution, it does not capture the width of the posterior properly for all variables. In addition the inference does not perform well for the latent variables c_6 to c_{10} where the prior distribution dominates. This is however very likely due to the diagnostics not being sensitive enough to the small deviations represented by the higher latent variables. Note that they represent a significantly lower amount of the variance. These variables are however still required for the inference as the

¹*SurroBIER* is still in active development and not published yet. Contact Robert Köberl at robert.koeberl@ipp.mpg.de to get access to the development version.

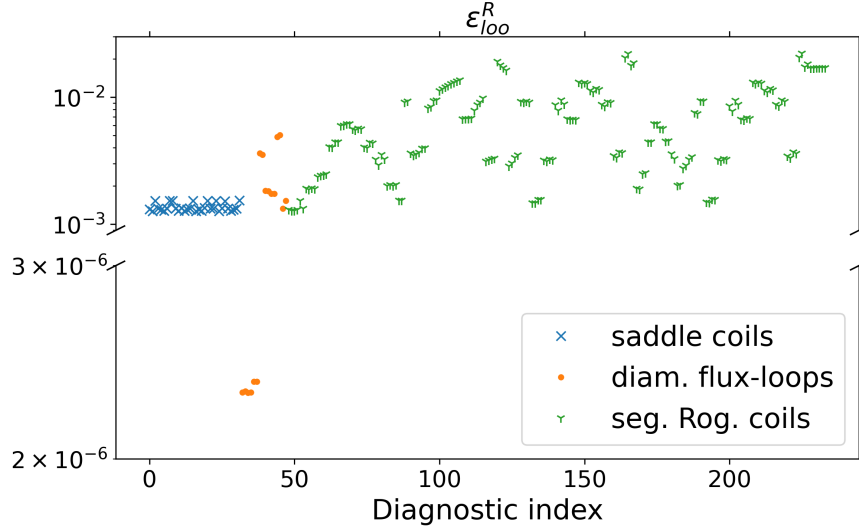


Figure 5.5: The leave-one-out error ε_{loo}^R [29] for each synthetic diagnostic PCE surrogate model relative to the variance of the training data. Reproduced from Köberl, Babin, and Albert [18].

correlation between the different latent variables can be inferred. While the correlations are not visible in Figure 5.6, a lower number of dimensions introduces higher errors from the dimensionality reduction, especially for the consistent pressure and current profiles (Section 4.4).

The latent variables of the posterior distribution can be projected back to full MHD equilibria. The results of the inference for the flux surface geometry are shown in Figure 5.7 and for the total toroidal flux and rotational transform profile in Figures 5.8a and 5.8b. In addition to samples from the posterior distribution and the ground truth, the *maximum-a-posterior* (MAP) estimate is shown. The total toroidal flux ψ_0 is inferred within a very small region of uncertainty, compared to the prior range between -2.5 and -1.6 Wb. This coincides well with the reasoning for the high accuracy of the diamagnetic flux loop surrogate models, that they measure ψ_0 almost directly. Additionally, ψ_0 is strongly correlated with the first latent variable c_0 . In Figure 5.7, the low uncertainty of ψ_0 is visible as the plasma volume is inferred very narrowly. Additionally, the position of the magnetic axis, which correlates with the maximum pressure p_0 and the second latent variable c_1 , is also very narrowly determined. Together they fix most of the flux surface positions, while small differences in the shape, especially near the boundary can still be seen. The samples of the ι profile in Figure 5.8b also all show the same general shape with some small variability.

The consistent pressure and current profiles in Figure 5.9 show a rather broad distribution, but the overall shape is still determined. They also violate the constraints which were put on the profile priors, in particular the monotonicity is not preserved. In part this is a problem of the dimensionality reduction, as described in Section 4.4, but

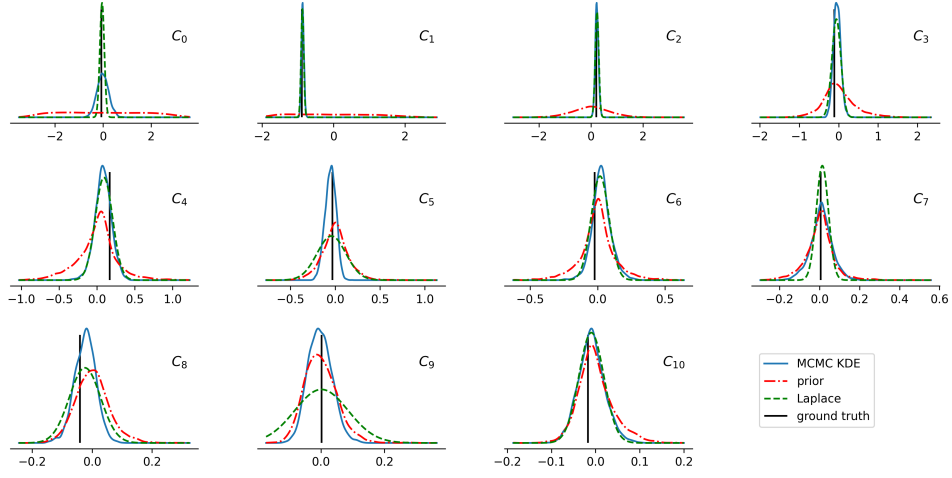


Figure 5.6: Results from the inference of a known ground truth for the latent variables c_0 to c_{10} , with the prior distribution (red), Laplace's approximation of the posterior (green) and KDEs of the posterior samples (blue) as well as the ground truth (black). Reproduced from Köberl, Babin, and Albert [18].

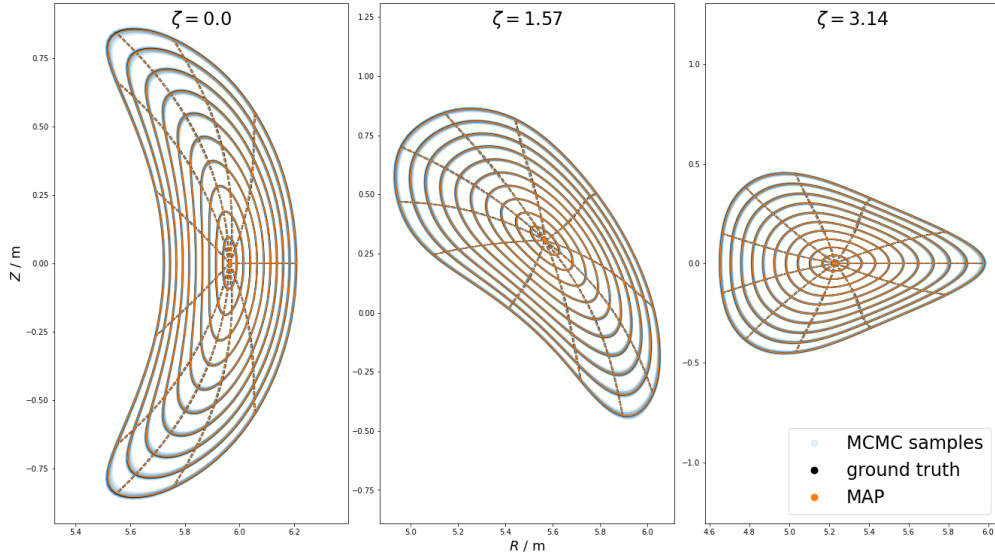


Figure 5.7: Results from the inference of a known ground truth for the flux surface geometry at three different toroidal angles ζ (in radians), defined by R , Z and λ , with the MAP estimate (orange), the posterior samples (transparent blue) as well as the ground truth (black). Reproduced from Köberl, Babin, and Albert [18].

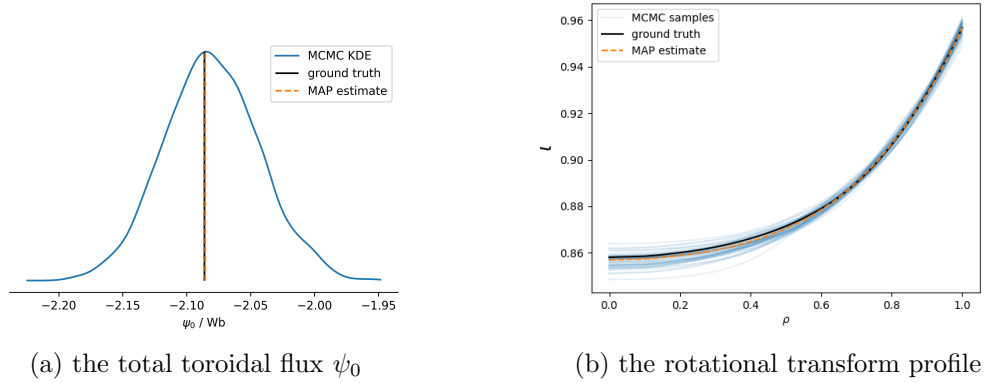


Figure 5.8: Results from the inference of a known ground truth for the total toroidal flux ψ_0 and rotational transform profile $\iota(\rho)$, with the MAP estimate (orange), the posterior samples (transparent blue) or their KDE (blue) as well as the ground truth (black). Reproduced from Köberl, Babin, and Albert [18].

the KDE and the approximation of independent distributions in the latent space likely contribute to this, by allowing the sampling of non-physical profiles.

5.5 Outlook

The results from Section 5.4 indicate that the presented framework is able to reconstruct the equilibrium defining parameters R, Z, λ, ι and ψ_0 from magnetic diagnostic signals. That is, the ground truth lies within the region of high probability of the posterior, which is narrow relative to the prior distribution. The MAP estimate also lies near the ground truth. Note however, that this study was done with a single synthetic sample without measurement error. Therefore further validation, especially with real experimental data, is necessary. While the consistent pressure and current profiles can be derived from the reconstructed parameters and the pressure profile fulfills the radial force balance (Equation 3.1.31) by construction, the profiles violate the physically motivated constraints regarding monotonicity and non-negativity defined in Section 5.2.

The new framework allows for a broad prior distribution of profiles and allows the exploration of the full posterior distribution, while keeping the computational costs low by using surrogate models and dimensionality reduction. A main benefit of the flow shown in Figure 5.1 is that it allows inference on equilibrium parameters directly. This makes the reconstruction an inverse problem again and typical Bayesian methods can be applied. The dimensionality of the latent space remains a crucial parameter, with which both the accuracy and the computational costs increase.

Therefore, most potential for further improvement likely lies with the dimensionality reduction. Possible improvements include a reweighing for the PCA or inclusion of additional parameters, as briefly shown in Section 4.5, but also replacing the linear PCA

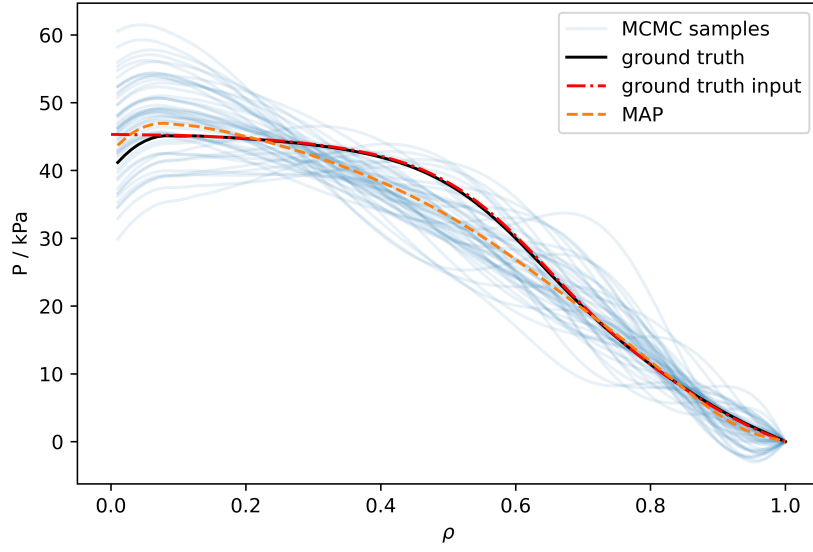


Figure 5.9: Results from the inference of a known ground truth for the consistent pressure profile p , with the MAP estimate (orange), the posterior samples (transparent blue) as well as the ground truth (black) and the input profiles for the ground truth calculation (red). Reproduced from Köberl, Babin, and Albert [18].

with a non-linear method, like a variational auto-encoder (VAE) [17]. A related topic of improvement is the choice of density estimation, which currently likely contributes significantly to the exploration of non-physical parts of the parameter space. Here however, the low number of samples in the comparatively high dimensional parameter space make this problem inherently difficult to solve. In the final application at an experimental device, it would however be possible to generate a much larger number of training samples as the same training data can likely be used for many experiments.

Summary

This thesis showed that data-driven dimensionality reduction of MHD equilibria is possible with simple Principal Component Analysis (PCA), at least for the device specific equilibrium prior needed in equilibrium reconstruction. While some error is introduced in the projection to the latent space, the corresponding consistent pressure and current profiles can be calculated, such that the radial force balance is fulfilled exactly. The number of latent dimensions controls the degree of error, but has a strong influence on the computational costs of applications. The benefit of additional latent dimensions seems to diminish smoothly, with no best choice of latent dimensions being easily determinable. Instead the number of latent dimensions needs to be determined by balancing the acceptable errors with the computational costs.

Tokamaks are a promising fusion reactor design, for which the toroidal axisymmetry simplifies many calculations. In Chapter 2, the Grad-Shafranov equation (Equation 2.1.40) was derived for the case of toroidal axisymmetry from the MHD equations introduced in Section 1.2. For the linear Solov'ev profiles for $p(\Psi)$ and $F^2(\Psi)$, there exist analytical solutions to the Grad-Shafranov equation [4]. They can be well represented with a 7 or 12-dimensional vector space constructed of simple, mostly polynomial basis functions. Each equilibrium can also be characterized by a number of meaningful parameters, like the inverse aspect ratio ϵ , elongation κ , triangularity δ or X-point position x_{sep} and y_{sep} . While the solution space is low-dimensional and can therefore be explored easily, the linearity restriction on the profiles is very limiting and usually not fulfilled in experiment. Despite this, these MHD equilibria, for example shown in Figure 2.1, can still approximate the flux surface geometries of real experiments and are well suited for preliminary investigations with simpler equilibria, before advancing to more complicated and more realistic equilibria from other sources. In the course of this work, parts of the equilibrium reconstruction framework presented in Chapter 5 were initially tested with these simpler equilibria for Solov'ev profiles.

The magnetic flux coordinates introduced in Section 1.4 are a common choice to represent the flux surface geometry and therefore magnetic field, for the more complicated 3D MHD equilibria of stellarators. In Chapter 3, the radial force balance (Equation 3.1.31) was derived as a weak formulation of the MHD momentum equation. By rearranging the terms, it is possible to calculate the consistent pressure profile to a given flux surface geometry. This is a central idea of the dimensionality reduction of MHD equilibria presented in this thesis: It is only necessary to describe and reduce the dimensionality of the flux surface geometry, the pressure and current profiles, which match this geometry, can be calculated rather quickly. This also guarantees that the radial force balance is always fulfilled.

Chapter 4 described the dimensionality reduction of equilibrium parameters, with the core ideas, to use Principal Component Analysis (PCA) to identify the linear subspace which most accurately approximates the distribution of parameters and to calculate the consistent profiles that match the flux surface geometry. The quality of this method was analyzed in Section 4.4 extensively. For the investigated dataset, 11 latent dimensions are enough to represent the flux surface geometry, but the corresponding consistent profiles can deviate from the original profiles by large amounts (Figure 4.8). 34 latent dimensions are found to provide an accurate representation of the flux surface geometry and a rough approximation of the consistent profiles. Finally, with 100 latent dimensions the consistent profiles mostly match the original profiles, but this dimensionality is too high for many applications.

For the 3D equilibrium reconstruction in Wendelstein 7-X developed by Köberl, Babin, and Albert [18], which was described in Chapter 5, the dimensionality reduction with 11 latent dimensions was used. The validation with a single unperturbed ground truth equilibrium performed well, with an accurate determination of the flux surface positions and a rough determination of the pressure profile, where the ground truth profile lies well within the region of high probability (Figure 5.7 to 5.9). The dimensionality reduction is crucial for this application, as it enables the use of surrogate models for the synthetic diagnostics, which greatly reduce the computational costs of the forward model, and make it unnecessary to rerun the MHD equilibrium solver on the reconstructed profiles. Instead, the reconstruction can be performed directly on the equilibrium parameters using Bayesian Inference.

Bibliography

- [1] O. Abril-Pla et al. “PyMC: A Modern, and Comprehensive Probabilistic Programming Framework in Python”. In: *PeerJ Computer Science* 9 (Sept. 2023), e1516. ISSN: 2376-5992. DOI: [10.7717/peerj-cs.1516](https://doi.org/10.7717/peerj-cs.1516).
- [2] T. Andreeva et al. “Equilibrium Evaluation for Wendelstein 7-X Experiment Programs in the First Divertor Phase”. In: *Fusion Engineering and Design* 146 (Sept. 2019), pp. 299–302. ISSN: 09203796. DOI: [10.1016/j.fusengdes.2018.12.050](https://doi.org/10.1016/j.fusengdes.2018.12.050).
- [3] G. Blatman and B. Sudret. “Adaptive Sparse Polynomial Chaos Expansion Based on Least Angle Regression”. In: *Journal of Computational Physics* 230.6 (Mar. 2011), pp. 2345–2367. ISSN: 00219991. DOI: [10.1016/j.jcp.2010.12.021](https://doi.org/10.1016/j.jcp.2010.12.021).
- [4] A. J. Cerfon and J. P. Freidberg. ““One Size Fits All” Analytic Solutions to the Grad–Shafranov Equation”. In: *Physics of Plasmas* 17.3 (Mar. 2010), p. 032502. ISSN: 1070-664X, 1089-7674. DOI: [10.1063/1.3328818](https://doi.org/10.1063/1.3328818).
- [5] M. R. Cianciosa, J. D. Hanson, and D. A. Maurer. “Uncertainty Analysis in 3D Equilibrium Reconstruction”. In: *Fusion Science and Technology* 74.1-2 (Aug. 2018), pp. 1–12. ISSN: 1536-1055, 1943-7641. DOI: [10.1080/15361055.2017.1392819](https://doi.org/10.1080/15361055.2017.1392819).
- [6] W. D. D’haeseleer et al. *Flux Coordinates and Magnetic Field Structure*. Berlin, Heidelberg: Springer Berlin Heidelberg, 1991. ISBN: 978-3-642-75597-2 978-3-642-75595-8. DOI: [10.1007/978-3-642-75595-8](https://doi.org/10.1007/978-3-642-75595-8).
- [7] D. W. Dudt and E. Kolemen. “DESC: A Stellarator Equilibrium Solver”. In: *Physics of Plasmas* 27.10 (Oct. 2020), p. 102513. ISSN: 1070-664X. DOI: [10.1063/5.0020743](https://doi.org/10.1063/5.0020743).
- [8] M. Endler et al. “Engineering Design for the Magnetic Diagnostics of Wendelstein 7-X”. In: *Fusion Engineering and Design* 100 (2015), pp. 468–494. ISSN: 0920-3796. DOI: [10.1016/j.fusengdes.2015.07.020](https://doi.org/10.1016/j.fusengdes.2015.07.020).
- [9] V. Eslbauer. “Two Analytical Solutions to the Grad-Shafranov Equation Using Solov’ev Pressure and Poloidal Current Profiles”. Bachelor’s Thesis. Graz: Graz University of Technology, Nov. 2017.
- [10] J. Feinberg and H. P. Langtangen. “Chaospy: An Open Source Tool for Designing Methods of Uncertainty Quantification”. In: *Journal of Computational Science* 11 (Nov. 2015), pp. 46–57. ISSN: 1877-7503. DOI: [10.1016/j.jocs.2015.08.008](https://doi.org/10.1016/j.jocs.2015.08.008).
- [11] R. Fischer et al. “Estimation and Uncertainties of Profiles and Equilibria for Fusion Modeling Codes”. In: *Fusion Science and Technology* 76.8 (Nov. 2020), pp. 879–893. ISSN: 1536-1055, 1943-7641. DOI: [10.1080/15361055.2020.1820794](https://doi.org/10.1080/15361055.2020.1820794).

- [12] R. Fischer et al. “Integrated Data Analysis of Profile Diagnostics at ASDEX Upgrade”. In: *Fusion Science and Technology* 58.2 (Oct. 2010), pp. 675–684. ISSN: 1536-1055, 1943-7641. DOI: [10.13182/FST10-110](https://doi.org/10.13182/FST10-110).
- [13] J. P. Freidberg. *Ideal MHD*. New York: Cambridge University Press, 2014. ISBN: 978-1-107-00625-6.
- [14] H. Grad and H. Rubin. “Hydromagnetic Equilibria and Force-Free Fields”. In: *Proceedings of the second United Nations international conference on the peaceful uses of atomic energy* 31 (Sept. 1958).
- [15] S. P. Hirshman and J. C. Whitson. “Steepest-descent Moment Method for Three-dimensional Magnetohydrodynamic Equilibria”. In: *Physics of Fluids* 26.12 (Dec. 1983), pp. 3553–3568. ISSN: 0031-9171. DOI: [10.1063/1.864116](https://doi.org/10.1063/1.864116).
- [16] S. Hoyer and J. Hamman. “Xarray: N-D Labeled Arrays and Datasets in Python”. In: *Journal of Open Research Software* 5.1 (2017). DOI: [10.5334/jors.148](https://doi.org/10.5334/jors.148).
- [17] D. P. Kingma and M. Welling. *Auto-Encoding Variational Bayes*. May 2014. arXiv: [1312.6114](https://arxiv.org/abs/1312.6114) [cs, stat].
- [18] R. Köberl, R. Babin, and C. G. Albert. “Magnetohydrodynamic Equilibrium Reconstruction with Consistent Uncertainties”. In: *Physical Sciences Forum*. Vol. 9. Garching, Germany: MDPI, Nov. 2023, p. 6. DOI: [10.3390/psf2023009006](https://doi.org/10.3390/psf2023009006).
- [19] R. Köberl et al. “Uncertainty Quantification in Three-Dimensional Magnetohydrodynamic Equilibrium Reconstruction via Surrogate-Assisted Bayesian Inference”. In: *Contributions to Plasma Physics* (2023), e202200173. ISSN: 1521-3986. DOI: [10.1002/ctpp.202200173](https://doi.org/10.1002/ctpp.202200173).
- [20] I. Kobyzev, S. J. Prince, and M. A. Brubaker. “Normalizing Flows: An Introduction and Review of Current Methods”. In: *IEEE Transactions on Pattern Analysis and Machine Intelligence* 43.11 (Nov. 2021), pp. 3964–3979. ISSN: 0162-8828, 2160-9292, 1939-3539. DOI: [10.1109/TPAMI.2020.2992934](https://doi.org/10.1109/TPAMI.2020.2992934).
- [21] S. Lazerson, S. Sakakibara, and Y. Suzuki. “A Magnetic Diagnostic Code for 3D Fusion Equilibria”. In: *Plasma Physics and Controlled Fusion* 55.2 (Feb. 2013), p. 025014. ISSN: 0741-3335, 1361-6587. DOI: [10.1088/0741-3335/55/2/025014](https://doi.org/10.1088/0741-3335/55/2/025014).
- [22] S. Lazerson and the DIII-D Team. “Three-Dimensional Equilibrium Reconstruction on the DIII-D Device”. In: *Nuclear Fusion* 55.2 (Feb. 2015), p. 023009. ISSN: 0029-5515, 1741-4326. DOI: [10.1088/0029-5515/55/2/023009](https://doi.org/10.1088/0029-5515/55/2/023009).
- [23] W. von der Linden, V. Dose, and U. von Toussaint. *Bayesian Probability Theory: Applications in the Physical Sciences*. Cambridge: Cambridge University Press, June 2014. ISBN: 978-1-139-56560-8. DOI: [10.1017/CB09781139565608](https://doi.org/10.1017/CB09781139565608).
- [24] A. Merlo et al. “Proof of Concept of a Fast Surrogate Model of the VMEC Code via Neural Networks in Wendelstein 7-X Scenarios”. In: *Nuclear Fusion* 61.9 (Sept. 2021), p. 096039. ISSN: 0029-5515, 1741-4326. DOI: [10.1088/1741-4326/ac1a0d](https://doi.org/10.1088/1741-4326/ac1a0d).
- [25] D. C. Montgomery and D. A. Tidman. “The BBGKY Kinetic Theory”. In: *Plasma Kinetic Theory*. McGraw-Hill, 1964, pp. 41–50.

- [26] A. Pavone et al. “Neural Network Approximation of Bayesian Models for the Inference of Ion and Electron Temperature Profiles at W7-X”. In: *Plasma Physics and Controlled Fusion* 61.7 (July 2019), p. 075012. ISSN: 0741-3335, 1361-6587. DOI: [10.1088/1361-6587/ab1d26](https://doi.org/10.1088/1361-6587/ab1d26).
- [27] C. E. Rasmussen and C. K. I. Williams. *Gaussian Processes for Machine Learning*. Adaptive Computation and Machine Learning. Cambridge, Mass: MIT Press, 2006. ISBN: 978-0-262-18253-9.
- [28] M. Sanders et al. “Analysis of the Motional Stark Effect (MSE) Diagnostic to Measure the Rotational Transform and Current Profile in the Large Helical Device”. In: *Review of Scientific Instruments* 92.5 (May 2021), p. 053503. ISSN: 0034-6748, 1089-7623. DOI: [10.1063/5.0018859](https://doi.org/10.1063/5.0018859).
- [29] R. Schobi, B. Sudret, and J. Wiart. “Polynomial-Chaos-Based Kriging”. In: *International Journal for Uncertainty Quantification* 5.2 (2015), pp. 171–193. ISSN: 2152-5080. DOI: [10.1615/Int.J.UncertaintyQuantification.2015012467](https://doi.org/10.1615/Int.J.UncertaintyQuantification.2015012467).
- [30] V. D. Shafranov. “Equilibrium of a Plasma Toroid in a Magnetic Field”. In: *Journal of Experimental and Theoretical Physics* 37 (Oct. 1959).
- [31] V. D. Shafranov. “Equilibrium of a Toroidal Pinch in a Magnetic Field”. In: *Soviet Atomic Energy* 13.6 (Nov. 1963), pp. 1149–1158. ISSN: 1573-8205. DOI: [10.1007/BF01312317](https://doi.org/10.1007/BF01312317).
- [32] L. S. Solov’ev. “The Theory of Hydromagnetic Stability of Toroidal Plasma Configurations”. In: *Soviet Journal of Experimental and Theoretical Physics* 26 (Feb. 1968), p. 400. ISSN: 1063-7761.
- [33] B. A. Stickler and E. Schachinger. *Basic Concepts in Computational Physics*. 2nd ed. Cham: Springer International Publishing, 2016. ISBN: 978-3-319-27263-4 978-3-319-27265-8. DOI: [10.1007/978-3-319-27265-8](https://doi.org/10.1007/978-3-319-27265-8).
- [34] U. Stroth. *Plasmaphysik: Phänomene, Grundlagen und Anwendungen*. 2nd ed. Berlin, Heidelberg: Springer Spektrum, Dec. 2017. ISBN: 978-3-662-55236-0. DOI: [10.1007/978-3-662-55236-0](https://doi.org/10.1007/978-3-662-55236-0).
- [35] J. Svensson and A. Werner. “Large Scale Bayesian Data Analysis for Nuclear Fusion Experiments”. In: *2007 IEEE International Symposium on Intelligent Signal Processing*. Alcalá de Henares, Spain: IEEE, 2007, pp. 1–6. ISBN: 978-1-4244-0829-0. DOI: [10.1109/WISP.2007.4447579](https://doi.org/10.1109/WISP.2007.4447579).

List of Figures

| | | |
|-----|------------------------------------------------------------------------------------------------------------------------------------------------------------------------------------------------------------------------------------------------------------------------------------------------------------------------------------------------------------------------------------------------------------------------------------------------------------------|----|
| 2.1 | The reference surface for the poloidal cross section of the plasma boundary, with the outer and inner equatorial points as well as the high point marked, alongside the surfaces of constant flux Ψ for MHD equilibria with top-down symmetry and no X-points, two X-points and a non-symmetric equilibrium with a single X-point. | 26 |
| 4.1 | Explained variance ratio σ_{evr}^2 of the i -th principal component (left) and unexplained variance ratio σ_{uvr}^2 for the projection to L latent dimensions (right). | 37 |
| 4.2 | Median relative L^2 -error for the total toroidal flux ψ_0 , the inverse coordinate maps R, Z and λ , the rotational transform ι , pressure gradient $\frac{dp}{d\rho}$, toroidal current I_{tor} and partial poloidal current \tilde{I}_{pol} profiles as functions of the number of latent dimensions L | 37 |
| 4.3 | Histogram of the relative L^2 -error (Equation 4.4.2) for the total toroidal flux ψ_0 , the inverse coordinate maps R, Z and λ , the rotational transform ι , pressure gradient $\frac{dp}{d\rho}$, toroidal current I_{tor} and partial poloidal current \tilde{I}_{pol} profiles for 11 latent dimensions, corresponding to 99.99% of the explained variance. The black dashed line shows the median of each distribution. | 38 |
| 4.4 | Histogram of the absolute L^2 -error (Equation 4.4.1) for the total toroidal flux ψ_0 , the inverse coordinate maps R, Z and λ , the rotational transform ι , pressure gradient $\frac{dp}{d\rho}$, toroidal current I_{tor} and partial poloidal current \tilde{I}_{pol} profiles 11 latent dimensions, corresponding to 99.99% of the explained variance. The black dashed line shows the median of each distribution. | 39 |
| 4.5 | Comparison of the explained variance ratio σ_{evr}^2 of the principal component i for the PCA of the inverse coordinate maps R, Z and λ as well as the rotational transform ι individually. | 39 |
| 4.6 | Histogram of the absolute and relative L^2 -error (Equation 4.4.1 and 4.4.2) as well as the magnitude $ Q $ for the covariant poloidal and toroidal magnetic field components B_ϑ and B_ζ , their integrals over flux surfaces and subsequent radial derivatives for 11 latent dimensions. Additionally, the relative L^2 -error of the pressure gradient profile (Equation 3.1.32) is shown. | 41 |
| 4.7 | Median relative L^2 -error for the consistent pressure gradient $\frac{dp}{d\rho}$, toroidal current I_{tor} and partial poloidal current \tilde{I}_{pol} profiles for varying poloidal and toroidal resolution. | 42 |

| | | |
|------|------------------------------------------------------------------------------------------------------------------------------------------------------------------------------------------------------------------------------------------------------------------------------------------------------------------------------------------------------------------------------------------------------------------------------------------------------------------------------------------------------------------------------------------------------------------------------|----|
| 4.8 | Visual comparison of the flux surface geometry (top left and top middle), containing the inverse coordinate maps R, Z and λ , the rotational transform ι (top right), pressure gradient $\frac{dp}{d\rho}$ (bottom left), toroidal current I_{tor} (bottom middle) and poloidal current \tilde{I}_{pol} (bottom right) profiles for a single equilibrium reduced to different number of latent dimensions L | 43 |
| 4.9 | Median relative L^2 -error for the total toroidal flux ψ_0 , the inverse coordinate maps R, Z and λ , the rotational transform ι , expanded and consistent pressure gradient $\frac{dp}{d\rho}_{\text{PCA}}$ and $\frac{dp}{d\rho}_{\text{findiff}}$, toroidal current I_{tor} and partial poloidal current \tilde{I}_{pol} profiles as functions of the weight of $\frac{dp}{d\rho}$ in the PCA with $L = 11$ latent dimensions. | 44 |
| 4.10 | Median relative L^2 -error for the total toroidal flux ψ_0 , the inverse coordinate maps R, Z and λ , the rotational transform ι , consistent and included pressure gradient $\frac{dp}{d\rho}$ and $\frac{dp}{d\rho}_{\text{PCA}}$, toroidal current I_{tor} and partial poloidal current \tilde{I}_{pol} profiles as functions of the number of principal components L for a PCA including $\frac{dp}{d\rho}$ with equal weight. The transparent lines show the error without including $\frac{dp}{d\rho}$ in the PCA. | 44 |
| 4.11 | Comparison of the included and consistent pressure gradient $\frac{dp}{d\rho}_{\text{PCA}}$ and $\frac{dp}{d\rho}_{\text{con}}$ with the original pressure gradient of a single sample for 11 and 34 latent dimensions corresponding to an unexplained variance ratio of 10^{-3} and 10^{-5} respectively. The original $\frac{dp}{d\rho}$ profile was included in the PCA with equal weight. | 45 |
| 5.1 | Overview of the proposed framework. Reproduced from Köberl, Babin, and Albert [18]. | 50 |
| 5.2 | Samples drawn from the prior distribution of the normalized pressure and toroidal current profiles. Reproduced from Köberl, Babin, and Albert [18]. | 53 |
| 5.3 | Rotational transform profile $\iota(\rho)$, flux surface geometry at the toroidal angle $\zeta = \pi$ and consistent pressure gradient profile $\frac{dp}{d\rho}(\rho)$ for the mean vector (black) and the positive and negative standard deviation in latent space for the first three principal components c_0 to c_2 . The value of the total toroidal flux ψ_0 is given in the legend. | 54 |
| 5.4 | The flux surfaces of a standard MHD equilibrium configuration of W7-X together with saddle coils (black), diamagnetic flux loops (green) and segmented Rogowski coils (blue). Image courtesy of Robert Köberl. | 55 |
| 5.5 | The leave-one-out error $\varepsilon_{\text{loo}}^R$ [29] for each synthetic diagnostic PCE surrogate model relative to the variance of the training data. Reproduced from Köberl, Babin, and Albert [18]. | 56 |
| 5.6 | Results from the inference of a known ground truth for the latent variables c_0 to c_{10} , with the prior distribution (red), Laplace's approximation of the posterior (green) and KDEs of the posterior samples (blue) as well as the ground truth (black). Reproduced from Köberl, Babin, and Albert [18]. | 57 |

| | | |
|-----|------------------------------------------------------------------------------------------------------------------------------------------------------------------------------------------------------------------------------------------------------------------------------------------------------------------------------------------------------|----|
| 5.7 | Results from the inference of a known ground truth for the flux surface geometry at three different toroidal angles ζ (in radians), defined by R , Z and λ , with the MAP estimate (orange), the posterior samples (transparent blue) as well as the ground truth (black). Reproduced from Köberl, Babin, and Albert [18]. | 58 |
| 5.8 | Results from the inference of a known ground truth for the total toroidal flux ψ_0 and rotational transform profile $\iota(\rho)$, with the MAP estimate (orange), the posterior samples (transparent blue) or their KDE (blue) as well as the ground truth (black). Reproduced from Köberl, Babin, and Albert [18]. | 58 |
| 5.9 | Results from the inference of a known ground truth for the consistent pressure profile p , with the MAP estimate (orange), the posterior samples (transparent blue) as well as the ground truth (black) and the input profiles for the ground truth calculation (red). Reproduced from Köberl, Babin, and Albert [18]. | 59 |

List of Tables

| | | |
|-----|-------------------------------------------------------------------------------------------------------------|----|
| 5.1 | The chosen prior parameters and their distribution. Reproduced from Köberl, Babin, and Albert [18]. | 52 |
|-----|-------------------------------------------------------------------------------------------------------------|----|

List of Code Listings

| | | |
|-----|-------------------------------------------------------|----|
| 4.1 | Example code using the <i>EqDist</i> package. | 47 |
|-----|-------------------------------------------------------|----|